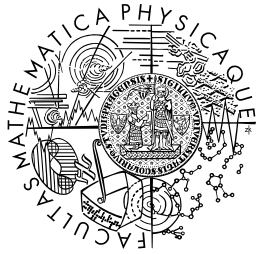

FACULTY
OF MATHEMATICS
AND PHYSICS
Charles University

BACHELOR THESIS

Jan Zlatník

Theory of electron photodetachment from molecular anion

Institute of Theoretical Physics

Supervisor of the bachelor thesis: doc. RNDr. Martin Čížek, PhD.
Study programme: Physics

Prague 2024

I declare that I carried out this bachelor thesis independently, and only with the cited sources, literature and other professional sources. It has not been used to obtain another or the same degree.

I understand that my work relates to the rights and obligations under the Act No. 121/2000 Sb., the Copyright Act, as amended, in particular the fact that the Charles University has the right to conclude a license agreement on the use of this work as a school work pursuant to Section 60 subsection 1 of the Copyright Act.

In ..... date ....

Author's signature

I am immensely thankful to my supervisor, doc. RNDr. Martin Čížek, PhD., for his expert guidance, thorough consultations, patience, and the time he invested in me during the writing of this thesis. My deep appreciation also goes to my parents for their encouragement and support throughout my studies.

Title: Theory of electron photodetachment from molecular anion

Author: Jan Zlatník

Institute: Institute of Theoretical Physics

Supervisor: doc. RNDr. Martin Čížek, PhD., Institute of Theoretical Physics

Abstract: In this thesis, we utilize the discrete-state-in-continuum model and projection operator formalism, successfully used to describe inelastic electron-molecule collisions, to model resonant electron photodetachment. An integral part of this work is the development of numerical methods that enable the quantitative evaluation of resonant electron photodetachment. Additionally, we seek analogs in photodetachment physics to phenomena observed in electron-molecule collisions, such as boomerang oscillations. The study utilizes these methods on simplified diatomic molecule models, particularly inspired by LiH and N_2 molecules. The findings suggest the potential for extending these numerical methods to more complex molecular systems in future research.

Keywords: Electron photodetachment, resonance, Schrödinger equation, discrete-state-in-continuum model, numerical methods

Název práce: Teorie odtržení elektronu z molekulárního aniontu

Autor: Jan Zlatník

Ústav: Ústav teoretické fyziky

Vedoucí bakalářské práce: doc. RNDr. Martin Čížek, PhD., Ústav teoretické fyziky

Abstrakt: V této práci využíváme model diskrétního stavu v kontinuu a formalismus projekčních operátorů, které se úspěšně používají pro popis nepružných srážek elektronu s molekulou, k modelování rezonančního elektronového fotodetachmentu. Součástí této práce je vývoj numerických metod, které umožňují výpočet rezonančního elektronového photodetachmentu. Dále v práci hledáme ve fyzice fotodetachmentu analogie k jevům pozorovaným při srážkách elektronu s molekulami, jako jsou boomerangové oscilace. Studie aplikuje tyto metody na zjednodušených modelech diatomických molekul, inspirovaných molekulami LiH a N_2. Výsledky práce vykazují potenciál pro rozšíření těchto numerických metod na složitější molekulární systémy v budoucím výzkumu.

Klíčová slova: Elektronový fotodetachment, rezonance, Schrödingerova rovnice, model diskrétního stavu v kontinuu, numerické metody

Contents

Introduction

Electron photodetachment is a process in which a molecular anion decays into a neutral molecule and an electron after absorbing a photon. In resonance photodetachment, the amplitude of this process can be amplified or reduced by the presence of a meta-stable anion state.

This thesis aims to develop numerical methods for calculating the amplitude of the resonance photodetachment process. We utilize the non-local discrete-state-in-continuum model and projection-operator formalism, approaches that have proven very successful in describing low-energy inelastic electron-molecule collisions leading to vibrational excitation, as discussed in sources such as [1]. In this thesis, we also address the vibrational excitation to draw comparisons with the photodetachment process.

In our study, we focus exclusively on diatomic molecules. We simplify the model by assuming only one excited meta-stable anion state and only one energetically accessible electronic state of the neutral molecule. Moreover, we consider only the first partial wave of the outgoing electron and photon absorption is treated in the dipole approximation. Although our description is simplified, it could potentially be extended to more complex systems in future work. The molecular models used in this study are significantly simplified and are intended to provide qualitative insights into molecular dynamics rather than a precise quantitative description of specific molecules.

In the first chapter, we describe the photodetachment process, explain the fundamental concepts used to theoretically address the inelastic resonance photodetachment, and derive the equations that this thesis aims to solve. Additionally, we introduce the fixed-nuclei approximation, which simplifies the resonance photodetachment process by neglecting the nuclear dynamics.

The second chapter is divided into three parts. The first part details how to reformulate the integro-differential equation for the photodetachment amplitude into a system of linear equations. The second part describes the numerical methods and procedures used in our computations. In the last part, we delve into the numerical properties of our approach, discussing its limitations as well as the convergence properties of our numerical methods.

In the final chapter, we apply our numerical methods to two molecular models. The first model, inspired by the LiH molecule, serves as a test model on which the numerical methods were developed. We use this model to explain several physical phenomena and to analyze the accuracy of the fixed-nuclei approximation. The model inspired by the N_2 molecule is used to test the developed numerical methods in a different regime. Additionally, we investigate this model to determine whether the *boomerang oscillations* phenomenon, observed in vibrational excitation by electron scattering cross-sections, as described for example in [2], has its analog in the photodetachment process.

Chapter 1

Theory

In this chapter, we initially provide a fundamental description of the photodetachment process. We then outline the derivation of specific equations, with the primary goal of this thesis being the numerical solution of these equations. The derivations are largely taken from the article written by my supervisor [3].

1.1 Resonance photodetachment

Electron photodetachment is a process in which a photon γ is absorbed by a molecular anion M^-, resulting in the decay of the anion into a neutral molecule M and an electron e^-. Resonant photodetachment describes a more specific process, in which the absorption of a photon γ leads to the electronic excitation of the anion into a meta-stable state $(M^-)^*$, which undergoes vibronic dynamics and decays into the electron-molecule scattering continuum $e^- + M(\nu_f)$ [3]:

$$\gamma + M^- \rightarrow (M^-)^* \rightarrow e^- + M(\nu_f). \tag{1.1}$$

In this thesis we use the non-local discrete-state-in-continuum model to calculate the electron spectrum for the photodetachment. This method is very successful approach in the description of the low-energy inelastic electron-molecule collisions leading to vibrational excitation [1, 3]

$$e^- + M(\nu_i) \rightarrow (M^-)^* \rightarrow e^- + M(\nu_f), \tag{1.2}$$

which we also address here to compere the dynamics with the photodetachment process.

1.2 Dipole approximation

The initial state $|\mathbf{\Psi}_0\rangle$ for the photodetachment process is assumed to be the ground state of the molecular anion M^-, treated within the *Born-Oppenheimer approximation* [3]. The ground state wavefunction is a product of the vibrational and electronic part $|\mathbf{\Psi}_0\rangle = |\chi_0\rangle|\phi_0\rangle$, where $|\phi_0\rangle$ is the ground electronic state of the anion and the vibrational wavefunction $\chi_0(R)$ solves the stationary Schrödinger equation

$$\left[\hat{T}_N + V_0(R)\right] \chi_0(R) = E_0 \chi_0(R), \tag{1.3}$$

where $\hat{T}_N$ is the vibrational kinetic energy operator, $V_0(R)$ is the potential energy function depending on the nuclear geometry R and E_0 is the energy of the initial vibrational state $|\chi_0\rangle$ [3].

In this thesis, the photon absorption is approached through the dipole approximation with the goal of calculating the photodetachment amplitude

$$A = \langle \mathbf{\Psi}^{(-)} \,|\, \hat{D} \,|\, \mathbf{\Psi}_0 \rangle = \langle \mathbf{\Psi}^{(-)} \,|\, \hat{D} \,|\, \chi_0 \rangle |\phi_0\rangle, \tag{1.4}$$

where $\hat{D}$ denotes the electrostatic dipole operator and $|\mathbf{\Psi}^{(-)}\rangle$ represents the scattering wavefunction subjected to outgoing boundary condition fixing the final vibrational state of the neutral molecule $|\nu_f\rangle$ and the outgoing electron state $|\epsilon_f\rangle$ [3]. During this process, the total energy E is conserved according to the following relation

$$E = \varepsilon_\gamma + E_0 = \epsilon_f + E_{\nu_f}, \tag{1.5}$$

where ε_γ represents the photon energy and E_{ν_f} the vibrational energy of the final state of the neutral molecule [3].

1.3 Discrete-state-in-continuum model

To calculate the scattering wavefunction $|\mathbf{\Psi}^{(-)}\rangle$, the discrete-state-in-continuum model and the projection-operator formalism is used. We assume that there exists a diabatic basis in the Hilbert space of electrons with the fixed nuclei of the molecule which consists of discrete states and electron scattering continuum states [3]. In this thesis, two discrete states are considered: the ground state of the anion $|\phi_0\rangle$ and the excited meta-stable anion state $|\phi_1\rangle$, however, more discrete states could be in principle included.

We can define projector to the discrete state part of the electronic Hilbert space

$$\hat{\mathcal{Q}} \coloneqq \sum_d |\phi_d\rangle\langle\phi_d| \tag{1.6}$$

and the complementary operator projecting on the background electron continuum $e^- + M$ [3]

$$\hat{\mathcal{P}} \coloneqq \hat{I} - \hat{\mathcal{Q}}. \tag{1.7}$$

In this subspace, it is convenient to use a basis consisting of the solutions to the background scattering problem with the fixed nuclei electronic Hamiltonian $\hat{H}_{\mathrm{el}}$. This is done while considering that the neutral molecule has only one energetically accessible electronic state. Simultaneously, we assume only the

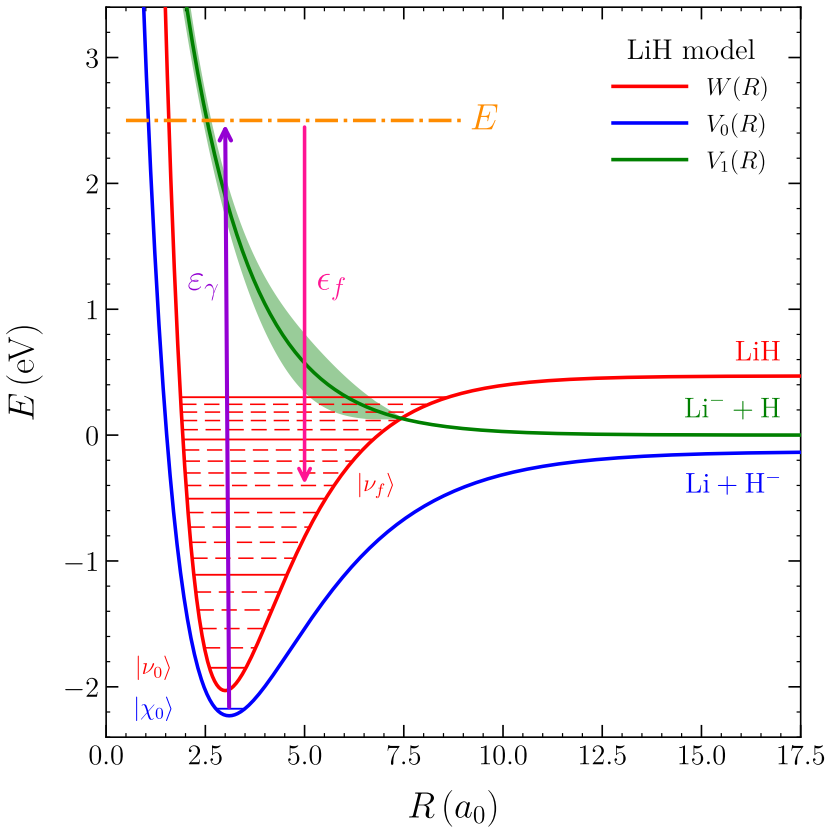

Figure 1.1 Schematic of the photodetachment process in the LiH model, as described in Appendix A. The diagram showcases potential curves for the neutral molecule $W(R)$, the ground state of the anion $V_0(R)$, and the electronically excited anion $V_1(R)$, which includes a depiction of the resonance width. Also depicted are the incoming photon energy ε_γ, the total conserving energy E, and the outgoing electron energy ϵ_f, illustrating the energy transitions and interactions within the photodetachment process.

first partial wave of the outgoing electron [3]

$$\hat{\mathcal{P}}\hat{H}_{\mathrm{el}}\hat{\mathcal{P}}|\epsilon\rangle = [W(R)+\epsilon]\,|\epsilon\rangle, \tag{1.8}$$

where $W(R)$ represents the energy of the ground electronic state of the neutral molecule and ϵ identifies the energy of the outgoing electron. Using this basis, we can express the projector onto the continuum part of the Hilbert space at a fixed R

$$\hat{\mathcal{P}} = \int |\epsilon\rangle\langle\epsilon|\,\mathrm{d}\epsilon. \tag{1.9}$$

The fixed nuclei Hamiltonian $\hat{H}_{\mathrm{el}}$ can be expanded in the aforementioned basis

$$\langle\phi_d\,|\,\hat{H}_{\mathrm{el}}\,|\,\phi_{d'}\rangle = V_d(R)\delta_{dd'}, \tag{1.10}$$

$$\langle\phi_d\,|\,\hat{H}_{\mathrm{el}}\,|\,\epsilon\rangle = V_{d\epsilon}(R)\delta_{d1}, \tag{1.11}$$

$$\langle\epsilon\,|\,\hat{H}_{\mathrm{el}}\,|\,\epsilon'\rangle = [W(R)+\epsilon]\,\delta(\epsilon-\epsilon'). \tag{1.12}$$

We assume that the bound state $|\phi_0\rangle$ is well isolated with non-crossing potentials $V_0(R)$ and $V_1(R)$, and therefore we neglect the coupling between the two discrete electronic states [3]. We also ignore the coupling between the ground state and the continuum, while the non-zero amplitude $V_{1\epsilon}(R)$ is responsible for electron autodetachment from the state $|\phi_1\rangle$ [3].

1.4 Vibrational excitation amplitude

The scattering wavefunction $|\mathbf{\Psi}^{(-)}\rangle$ can also be expanded in the basis constructed in section 1.3

$$|\mathbf{\Psi}^{(-)}\rangle = |\psi_1\rangle|\phi_1\rangle + \int |\psi_\epsilon\rangle|\epsilon\rangle\,\mathrm{d}\epsilon, \tag{1.13}$$

where the expansion into the ground state was omitted due to the previously mentioned decoupling [3]. In the case of the vibrational excitation process the T-matrix elements can be expressed as

$$T_{\mathrm{VE}} = \langle\mathbf{\Psi}^{(-)}\,|\,\hat{V}\,|\,\nu_i\rangle|\epsilon_i\rangle = \langle\psi_1\,|\,V_{1\epsilon_i}\,|\,\nu_i\rangle, \tag{1.14}$$

where $\hat{V} = \hat{\mathcal{P}}\hat{H}_{\mathrm{el}}\hat{\mathcal{Q}} + \hat{\mathcal{Q}}\hat{H}_{\mathrm{el}}\hat{\mathcal{P}}$ [3].

Components of the scattering wavefunction (1.13) can be determined by solving the stationary Schrödinger equation with Hamiltonian $\hat{H} = \hat{T}_N + \hat{H}_{\mathrm{el}}$, subject to appropriate boundary condition [3]

$$|\psi_1\rangle = 0 + [E-\hat{H}_1]^{-1}\int V_{1\epsilon}|\psi_\epsilon\rangle\,\mathrm{d}\epsilon, \tag{1.15}$$

$$|\psi_\epsilon\rangle = |\nu_f\rangle\delta(\epsilon - \epsilon_f) + [E - \hat{h}_0 - \epsilon]^{-1} V_{1\epsilon}|\psi_1\rangle, \tag{1.16}$$

where

$$\hat{H}_1 = \hat{T}_N + V_1(R), \tag{1.17}$$

$$\hat{h}_0 = \hat{T}_N + W(R) \tag{1.18}$$

and the final vibrational states of the neutral molecule are solution to the stationary Schrödinger equation

$$\hat{h}_0|\nu_f\rangle = E_{\nu_f}|\nu_f\rangle. \tag{1.19}$$

Substituting the equation (1.16) into (1.15) yields after formal rearrangement of terms

$$|\psi_1\rangle = [E - \hat{H}_1 - \hat{F}^\dagger(E - \hat{h}_0)]^{-1} V_{1\epsilon_f}|\nu_f\rangle, \tag{1.20}$$

with $\hat{F}(\varepsilon)$ defined as

$$\hat{F}(\varepsilon) \coloneqq \int_0^\infty V_{1\epsilon}(R)[\varepsilon - \epsilon + i\eta]^{-1} V_{1\epsilon}(R')\,\mathrm{d}\epsilon. \tag{1.21}$$

Using the equation (1.20), expression (1.14) can be rewritten as

$$T_{\mathrm{VE}} = \langle \nu_f \,|\, V_{1\epsilon_f}[E - \hat{H}_1 - \hat{F}(E - \hat{h}_0)]^{-1} V_{1\epsilon_i} \,|\, \nu_i\rangle. \tag{1.22}$$

From this formula, the cross-section of the vibrational excitation process can be also calculated

$$\sigma_{i\to f} = \frac{2\pi^3}{\epsilon_i}|T_{\mathrm{VE}}|^2. \tag{1.23}$$

1.5 Photodetachment amplitude

Analogously to equation (1.22), we aim to derive the expression for the photodetachment amplitude (1.4). However, in this case, it will be necessary also to consider the continuum component which we obtain by substituting equation (1.20) back into equation (1.16)

$$\begin{aligned} |\psi_\epsilon\rangle = {} & |\nu_f\rangle\delta(\epsilon - \epsilon_f) + \\ & + [E - \hat{h}_0 - \epsilon]^{-1} V_{1\epsilon}[E - \hat{H}_1 - \hat{F}^\dagger(E - \hat{h}_0)]^{-1} V_{1\epsilon_f}|\nu_f\rangle. \end{aligned} \tag{1.24}$$

We start by defining the fixed-R transition dipole moments for the discrete state $|\phi_1\rangle$ and the background continuum $|\epsilon\rangle$

$$\mu_1(R) \coloneqq \langle \phi_1 \,|\, \hat{D} \,|\, \phi_0\rangle, \tag{1.25}$$

$$\mu_\epsilon(R) \coloneqq \langle \epsilon \,|\, \hat{D} \,|\, \phi_0 \rangle. \tag{1.26}$$

Using these definitions, we can rewrite equation (1.4) as follows

$$A = \langle \psi_1 \,|\, \mu_1 \,|\, \chi_0 \rangle + \int \langle \psi_\epsilon \,|\, \mu_\epsilon \,|\, \chi_0 \rangle \, \mathrm{d}\epsilon. \tag{1.27}$$

By substituting equations (1.15), (1.24) into equation (1.27), we obtain the following expression for the components of the photodetachment amplitude, which are labeled separately for their physical interpretation. The total amplitude is then given by their sum $A = A_{\mathrm{dir}} + A_{\mathrm{res}} + A_{\mathrm{att}}$

$$A_{\mathrm{dir}} = \langle \nu_f \,|\, \mu_\epsilon \,|\, \chi_0 \rangle, \tag{1.28}$$

$$A_{\mathrm{res}} = \langle \nu_f \,|\, V_{1\epsilon_f} [E - \hat{H}_1 - \hat{F}(E - \hat{h}_0)]^{-1} \mu_1 \,|\, \chi_0 \rangle, \tag{1.29}$$

$$A_{\mathrm{att}} = \langle \nu_f \,|\, V_{1\epsilon_f} [E - \hat{H}_1 - \hat{F}(E - \hat{h}_0)]^{-1} \hat{M}(E - \hat{h}_0) \,|\, \chi_0 \rangle, \tag{1.30}$$

where we have defined, similarly to $\hat{F}(\varepsilon)$,

$$\hat{M}(\varepsilon) \coloneqq \int_0^\infty V_{1\epsilon}(R) [\varepsilon - \epsilon + i\eta]^{-1} \mu_e(R') \, \mathrm{d}\epsilon, \tag{1.31}$$

which can be interpreted as the transition amplitude through dipole transition to the continuum state $|\epsilon\rangle$ from which the electron is captured to the metastable anion state $|\phi_1\rangle$ [3].

The components of the photodetachment amplitude can be explained as follows: The *direct amplitude* A_{dir} (1.28) corresponds to the direct dipole photodetachment from the ground state to the background continuum [3]

$$\gamma + \mathrm{M}^- \to \mathrm{M}(\nu_f) + \mathrm{e}^-. \tag{1.32}$$

The *resonant amplitude* A_{res} (1.28) represents the dipole transition to the discrete state $|\phi_1\rangle$ followed by an autodetachment to the neutral molecule and the background continuum [3]

$$\gamma + \mathrm{M}^- \to (\mathrm{M}^-)^* \to \mathrm{M}(\nu_f) + \mathrm{e}^-. \tag{1.33}$$

Finally, the *attachment amplitude* A_{att} (1.30) describes a more complicated process in which the direct dipole photodetachment to intermediate continuum state is followed by electron capture to $|\phi_1\rangle$ and subsequently succeeded by an autodetachment [3]

$$\gamma + \mathrm{M}^- \to \mathrm{M}(\nu) + \mathrm{e}^- \to (\mathrm{M}^-)^* \to \mathrm{M}(\nu_f) + \mathrm{e}^-. \tag{1.34}$$

Assessing the relative importance of the aforementioned mechanisms is not straightforward.

1.6 Fixed-nuclei approximation

This section introduces the fixed-nuclei approximation, which simplifies the dynamics of molecular systems by assuming static nuclear positions R. We will examine its impact on photodetachment amplitudes and aim to draw comparisons with the full dynamical approach described in the previous section. In the fixed-nuclei approximation, we can rewrite the conservation of energy relation (1.5) as follows

$$E(R) = \varepsilon_\gamma + V_0(R) = \epsilon_f + W(R). \tag{1.35}$$

Similarly to (1.13), we can expand the scattering wavefunction at fixed R [3]

$$|\Psi^{(-)}(E)\rangle = \psi_1(R)|\phi_1\rangle + \int \psi_\epsilon(R)|\epsilon\rangle \, \mathrm{d}\epsilon, \tag{1.36}$$

where $\psi_1(R)$ and $\psi_\epsilon(R)$ are now R-dependent numbers, not wavefunctions in vibrational space [3]. Using the following parametrization of electronic Hamiltonian

$$\hat{H}_{\mathrm{el}} = |\phi_1\rangle V_1 \langle\phi_1| + \int |\epsilon\rangle[W + \epsilon]\langle\epsilon| \, \mathrm{d}\epsilon + \int [|\phi_1\rangle V_{1\epsilon}\langle\epsilon| + |\epsilon\rangle V_{1\epsilon}\langle\phi_1|] \, \mathrm{d}\epsilon, \tag{1.37}$$

the fixed-R scattering problem with $\hat{H}_{\mathrm{el}}$ can be solved to find the components [3]

$$\psi_1(R) = [E - V_1(R) - F(E - W(R))]^{-1} V_{1\epsilon_i}(R), \tag{1.38}$$

$$\psi_\epsilon(R) = \delta(\epsilon - \epsilon_i) + [E - \epsilon - W(R)]^{-1} V_{1\epsilon}(R)\psi_1(R). \tag{1.39}$$

It is noteworthy that in the fixed-nuclei approximation, the argument of the non-local level-shift operator F has shifted from $E - \hat{h}_0$ to $E - W(R)$, which corresponds to the electron energy relative to the scattering threshold [3].

To calculate the fixed-R moment function

$$\mu \coloneqq \langle \Psi^{(-)}(E) \,|\, \hat{D} \,|\, \phi_0 \rangle, \tag{1.40}$$

we substitute equations (1.38) and (1.39) into (1.36). Using the definitions of μ_1 (1.25) and μ_ϵ (1.26), we obtain the expression [3]

$$\mu = \mu_{\epsilon_f} + \frac{\mu_1 V_{1\epsilon_f}}{\epsilon_f - V_1 - F(E - W)} + \frac{M(E - W)V_{1\epsilon_f}}{\epsilon_f - V_1 - F(E - W)}. \tag{1.41}$$

It is important to note that μ is inherently R-dependent. For clarity, the notation indicating dependence on R has been omitted in the above formula. Moreover, the individual terms in the expression for the moment function μ

can be directly linked to the respective components of the photodetachment amplitude as outlined in equations (1.28), (1.29) and (1.30), specifically in the order: *direct*, *resonant* and *attachment* [3].

To compare the results of the fixed-nuclei approximation with the photodetachment amplitude that includes full dynamics, it is necessary to incorporate the distribution of the molecule across different internuclear separations R. This is accomplished by averaging the moment function $\mu(R)$ over all R with a weighting function given by the wave functions of the initial vibrational state of the anion $\chi_0(R)$ and the final vibrational state of the neutral molecule $\nu_f(R)$

$$A_{\mathrm{FN}}(\nu_f) \coloneqq \langle \nu_f \,|\, \mu \,|\, \chi_0 \rangle = \int \nu_f^*(R)\mu(R)\chi_0(R)\,\mathrm{d}R. \tag{1.42}$$

Furthermore, we can define the integral fixed-nuclei approximation amplitude for photodetachment (or its square) by summing over all final states. This process, after applying the resolution of the identity, yields the following simple formula

$$|A_{\mathrm{FN}}^{(\mathrm{int})}|^2 \coloneqq \sum_{\nu_f} \langle \chi_0 \,|\, \mu^* \,|\, \nu_f \rangle \langle \nu_f \,|\, \mu \,|\, \chi_0 \rangle = \int |\chi_0(R)|^2 |\mu(R)|^2 \,\mathrm{d}R. \tag{1.43}$$

Chapter 2

Numerical solution

This chapter addresses the numerical solution of equations for photodetachment and vibrational excitation amplitudes, formulated in the theoretical part 1. To make these equations suitable for numerical methods, we first need to reformulate them, which is the focus of the first section. The second section details the implementation of numerical methods used for solving them. The third examines their convergence and the accuracy of the results.

2.1 Reformulation of the problem

The equations for the *resonant* (1.29) and *attachment* (1.30) photodetachment amplitudes, as well as for the vibrational excitation amplitude (1.22), are all formulated in the general form

$$\langle \nu_f \,|\, V_{1\epsilon_f} [E - \hat{H}_1 - \hat{F}(E - \hat{h}_0)]^{-1} \,|\, \varphi \rangle, \tag{2.1}$$

where $|\varphi\rangle$ represents a distinct right-hand side specific to each amplitude type. In contrast, the *direct* photodetachment amplitude is more straightforward to compute. The formula (1.28) can be directly applied using standard methods discussed in Section 2.2, and no additional procedures are needed for its computation.

Firstly, we will focus on computing the operator inversion component $[E - \hat{H}_1 - \hat{F}(E - \hat{h}_0)]^{-1}$ applied to $|\varphi\rangle$ from the expression (2.1). This is equivalent to solving the following equation for $|\psi\rangle$

$$[E - \hat{H}_1 - \hat{F}(E - \hat{h}_0)]|\psi\rangle = |\varphi\rangle. \tag{2.2}$$

We rearrange this equation as

$$[E - \hat{H}_1]|\psi\rangle = |\varphi\rangle + \hat{F}(E - \hat{h}_0)|\psi\rangle \tag{2.3}$$

We can now formally define the retarded Green's operator $\hat{G}^{(+)}$ as the solution $|\zeta\rangle = \hat{G}^{(+)}|\xi\rangle$ to the equation $[E-\hat{H}_1]|\zeta\rangle = |\xi\rangle$, with the appropriate boundary condition for an outgoing wave. Using this definition, we reformulate the integro-differential Schrödinger-type equation (2.3) into the purely integral form of a distorted wave Lippmann-Schwinger equation

$$|\psi\rangle = \hat{G}^{(+)}|\varphi\rangle + \hat{G}^{(+)}\hat{F}(E-\hat{h}_0)|\psi\rangle. \tag{2.4}$$

Now it is time to tackle the non-local level-shift operator $\hat{F}$. To begin with, we assume that the fixed-R discrete-state-continuum coupling, as described in (1.11), can be written in a separable form [3]

$$V_{1\epsilon}(R) = g(R)f(\epsilon). \tag{2.5}$$

Thanks to this, we can rewrite the relationship given in (1.21) into the form

$$\hat{F}(\varepsilon) = g(R)\int_0^\infty \frac{f^2(\epsilon)}{\varepsilon-\epsilon+i\eta}\,\mathrm{d}\epsilon\, g(R') =: g(R)\,\hat{\mathcal{F}}(\varepsilon)\,g(R'). \tag{2.6}$$

Secondly, due to the argument of $\hat{F}$ being $E-\hat{h}_0$, we can express this operator in its spectral form using the spectrum of $\hat{h}_0$

$$\hat{\mathcal{F}}(E-\hat{h}_0) = \sum_{\nu'}|\nu'\rangle\mathcal{F}(E-E_{\nu'})\langle\nu'|, \tag{2.7}$$

where $\mathcal{F}$ is just a number given by the integral transform. Overall, can we represent the action of the operator $\hat{F}$ as

$$\hat{F}(E-\hat{h}_0) = \sum_{\nu'}\hat{g}|\nu'\rangle\mathcal{F}(E-E_{\nu'})\langle\nu'|\hat{g}. \tag{2.8}$$

Using the relation for $\hat{F}$ given in (2.8), we can rewrite the equation (2.4) into the following form

$$|\psi\rangle - \sum_{\nu'}\hat{G}^{(+)}\hat{g}|\nu'\rangle\mathcal{F}(E-E_{\nu'})\langle\nu'\,|\,\hat{g}\,|\,\psi\rangle = \hat{G}^{(+)}|\varphi\rangle. \tag{2.9}$$

Finally, we take the projection of this equation onto $\langle\nu|\hat{g}$

$$\langle\nu\,|\,\hat{g}\,|\,\psi\rangle - \sum_{\nu'}\langle\nu\,|\,\hat{g}\,\hat{G}^{(+)}\,\hat{g}\,|\,\nu'\rangle\mathcal{F}(E-E_{\nu'})\langle\nu'\,|\,\hat{g}\,|\,\psi\rangle = \langle\nu\,|\,\hat{g}\,\hat{G}^{(+)}\,|\,\varphi\rangle. \tag{2.10}$$

Now we see that the equation we obtained is a system of linear equations, which can be written in matrix form

$$[\mathbb{I}-\mathbb{G}\mathbb{F}]\boldsymbol{p} = \boldsymbol{r}, \tag{2.11}$$

where we have defined:

$$\mathbb{G}: \qquad G_{kl} \coloneqq \langle \nu_k \,|\, \hat{g}\, \hat{G}^{(+)}\, \hat{g} \,|\, \nu_l \rangle \tag{2.12}$$

$$\mathbb{F}: \qquad F_{kl} \coloneqq \delta_{kl} \mathcal{F}(E - E_{\nu_k}), \tag{2.13}$$

$$\boldsymbol{p}: \qquad p_k \coloneqq \langle \nu_k \,|\, \hat{g} \,|\, \psi \rangle, \tag{2.14}$$

$$\boldsymbol{r}: \qquad r_k \coloneqq \langle \nu_k \,|\, \hat{g}\, \hat{G}^{(+)} \,|\, \varphi \rangle, \tag{2.15}$$

and $\mathbb{I}$ is the identity matrix.

Given the definition of $|\psi\rangle$ in (2.4) and $\boldsymbol{p}$ in (2.14), it is now straightforward to see that the amplitudes satisfy

$$A_\bullet(\nu_f) = \langle \nu_f \,|\, V_{1\epsilon_f} \,|\, \psi_\bullet \rangle = f(\epsilon_f) \langle \nu_f \,|\, \hat{g} \,|\, \psi_\bullet \rangle = f(\epsilon_f) p_f, \tag{2.16}$$

where $A_\bullet$ stands for A_{res}, A_{att}, or T_{VE}, and $|\psi_\bullet\rangle$ respectively. Considering the form of the equation (2.11), the computation of individual amplitudes can be streamlined by solving the system of linear equations for any given right-hand side. This can be efficiently accomplished using LU decomposition and then applying the solution to different right-hand side vectors $\boldsymbol{r}_\bullet$. This process yields amplitudes for all final states simultaneously.

As for the right-hand side vectors, we derive respective expressions from the definitions of each amplitude (1.29), (1.30), (1.22). For the *resonant* and vibrational excitation amplitudes, their expressions are simple to evaluate

$$r_k^{(\mathrm{res})} = \langle \nu_k \,|\, \hat{g}\, \hat{G}^{(+)} \mu_1 \,|\, \chi_0 \rangle, \tag{2.17}$$

$$r_k^{(\mathrm{VE})} = \langle \nu_k \,|\, \hat{g}\, \hat{G}^{(+)} V_{1\epsilon_i} \,|\, \nu_i \rangle = f(\epsilon_i) \langle \nu_k \,|\, \hat{g}\, \hat{G}^{(+)} \hat{g} \,|\, \nu_i \rangle = (\mathbb{G} \boldsymbol{q}_{\mathrm{VE}})_k, \tag{2.18}$$

where we have used the definition of $\mathbb{G}$ (2.12) and have defined

$$\boldsymbol{q}_{\mathrm{VE}}: \qquad q_k^{(\mathrm{VE})} \coloneqq \delta_{ik} f(\epsilon_i). \tag{2.19}$$

Here, $|\nu_i\rangle$ corresponds to the initial vibrational state and ϵ_i to the initial electron energy during the vibrational excitation process. Finding the right-hand side vector for the *attachment* amplitude is a bit more complicated given the presence of the $\hat{M}$ operator. This can be addressed in the same manner as $\hat{F}$, by applying the procedure outlined between equations (2.5) and (2.8), assuming that the fixed-R transition dipole moment to the background continuum can be written in a separable form

$$\mu_\epsilon(R) = g_\mu(R) f_\mu(\epsilon). \tag{2.20}$$

Consequently, we derive an expression for the operator $\hat{M}$

$$\hat{M}(E - \hat{h}_0) = \sum_{\nu'} \hat{g} |\nu'\rangle \mathcal{M}(E - E_{\nu'}) \langle \nu' | \hat{g}_\mu, \tag{2.21}$$

where, analogously to $\hat{F}(\epsilon)$, we have defined

$$\hat{M}(\varepsilon) = g(R) \int_0^\infty \frac{f(\epsilon) f_\mu(\epsilon)}{\varepsilon - \epsilon + i\eta} \, \mathrm{d}\epsilon \, g_\mu(R') \coloneqq g(R) \hat{\mathcal{M}}(\varepsilon) g_\mu(R'). \tag{2.22}$$

Overall, this allows us to derive the expression for the right-hand side vector for the *attachment* amplitude

$$r_k^{(\mathrm{att})} = \sum_{\nu'} \langle \nu_k \,|\, \hat{g} \, \hat{G}^{(+)} \, \hat{g} \,|\, \nu' \rangle \mathcal{M}(E - E_{\nu'}) \langle \nu' \,|\, \hat{g}_\mu \,|\, \chi_0 \rangle = (\mathbb{G} \boldsymbol{q}_{\mathrm{att}})_k, \tag{2.23}$$

where we have again used the definition of $\mathbb{G}$ (2.12) and have defined

$$\boldsymbol{q}_{\mathrm{att}} : \qquad q_k^{(\mathrm{att})} \coloneqq \mathcal{M}(E - E_{\nu_k}) \langle \nu' \,|\, \hat{g}_\mu \,|\, \chi_0 \rangle. \tag{2.24}$$

2.2 Methods of numerical solution

For the purpose of numerical solution, we represent states $|\varphi\rangle$ in the vibrational Hilbert space as wavefunctions $\varphi(R) = \langle R \,|\, \varphi \rangle$ on a finite grid

$$\boldsymbol{R} \coloneqq (R_1, R_1 + \Delta R, \cdots, R_N - \Delta R, R_N), \tag{2.25}$$

where N is the number of grid points and $\Delta R = (R_N - R_1)/(N-1)$. Unless stated otherwise, we assume $R_1 = 0$. The choice of R_N will be discussed later.

The inner product of two states in the vibrational Hilbert space, represented as the integral of the corresponding wavefunctions over R, is given by

$$\langle \psi \,|\, \phi \rangle = \int_{R_1}^{R_N} \psi^*(R') \phi(R') \, \mathrm{d}R', \tag{2.26}$$

where the integration over $\boldsymbol{R}$ is evaluated using the trapezoidal rule

$$\int_{R_1}^{R_N} f(R') \, \mathrm{d}R' \approx \frac{\Delta R}{2} \left[f(R_1) + 2 \sum_{j=1}^{N-2} f(R_1 + j\Delta R) + f(R_N) \right]. \tag{2.27}$$

Integrations over other intervals are treated analogously.

The main system of linear equations (2.11) can be solved using any suitable software. Specifically, we have used the DGESV and ZGESV procedures from the LAPACK library [4] to solve it. To construct the system of linear equations' matrix and right-hand side vector, the following procedures must be implemented and will be discussed in the subsequent subsections:

- Finding eigen wavefunctions and energies in individual potentials.

- Determining the retarded Green's operator $\hat{G}^{(+)}$ with the appropriate boundary condition.
- Calculating the integral transforms $\mathcal{F}(\varepsilon)$ and $\mathcal{M}(\varepsilon)$.

Once these procedures have been established, we will have all the necessary ingredients to obtain the amplitudes for photodetachment and vibrational excitation.

2.2.1 Computation of eigenstates

For our calculations, we need to numerically find the vibrational wavefunctions $\nu(R)$ of the neutral molecule, which is described by the potential W, and the ground vibrational wavefunction $\chi_0(R)$ of the anion, described by the potential V_0. To solve this, we have implemented two procedures: grid discretization and the Four-DVR method. Both methods are expected to yield qualitatively similar results, yet they differ in their numerical properties.

We generally solve the stationary Schrödinger equation

$$\left[-\frac{\hbar^2}{2m}\frac{\mathrm{d}^2}{\mathrm{d}R^2} + V(R)\right]\psi(R) = E\psi(R), \tag{2.28}$$

where m is the reduced mass of the system. Due to the grid being finite, we impose artificial boundary conditions of the zero wavefunction outside the grid. The zero boundary condition at the origin R_1, can be understood as addressing only the s-wave component of the whole 3D problem. In this context, $\psi(R)/R$ is interpreted as the radial function for the s-wave, where a zero boundary condition at $R = 0$ is necessary. For bound states, we desire the wavefunction to decay exponentially as $R \to \infty$, hence the boundary condition at sufficiently large R_N is also natural. This fact is one of the limitations we impose on R_N, but this will be discussed later. For unbound states, this condition causes an artificial discretization of an otherwise continuous spectrum. The density of this discretization again relates to the choice of R_N and will be discussed later.

Grid discretisation The first method is based on the discretization of the second derivative in the kinetic energy operator. This is commonly done using a finite difference approach, where the second derivative is approximated by a difference formula. In our case, the central difference formula was used, which can be expressed as [5]

$$\frac{\mathrm{d}^2\psi}{\mathrm{d}R^2}(R) \approx \frac{\psi(R+\Delta R) - 2\psi(R) + \psi(R-\Delta R)}{(\Delta R)^2}, \tag{2.29}$$

where ΔR is the grid spacing. If we denote $\psi(R_1 + (j-1)\Delta R)$ as ψ_j, then the Schrödinger equation (2.28) translates into an eigenvalue equation for the eigenvalue E and the eigenvector $\boldsymbol{\psi} \coloneqq (\psi_1, \cdots, \psi_N)$ of the matrix $\mathbb{H}$

$$\mathbb{H}\boldsymbol{\psi} = E\boldsymbol{\psi}, \tag{2.30}$$

where $\mathbb{H}$ is an $(N \times N)$-dimensional tridiagonal matrix of the Hamiltonian with elements

$$H_{ij} = \frac{\hbar^2}{m}\frac{1}{(\Delta R)^2} + V(R_j) \qquad \text{for } i = j, \tag{2.31}$$

$$H_{ij} = -\frac{\hbar^2}{2m}\frac{1}{(\Delta R)^2} \qquad \text{for } |i-j| = 1 \tag{2.32}$$

and all other elements are zero. In this procedure, the previously mentioned artificial boundary conditions are implemented by essentially setting ψ_0 and ψ_{N+1} equal to zero.

To solve the eigenvalue problem (2.30), any suitable software can be used. In our implementation, the DSTEDC procedure from the LAPACK library [4], which is intended for the diagonalization of tridiagonal matrices, was utilized. As a result, we obtained the first N eigenenergies and eigenvectors, which correspond to the first N wavefunctions evaluated at the grid points $\boldsymbol{R}$. To ensure proper normalization, eigenvectors were multiplied by the factor $1/\sqrt{\Delta R}$.

The Fourier Discrete Variable Representation (Four-DVR) method is used to solve the Schrödinger equation (2.28) using the basis of particle-in-a-box wavefunctions [6]. The basis functions and corresponding energies, given by the following equations, are taken from [7]:

$$\varphi_n(R) = \sqrt{\frac{2}{L}}\sin\left[\frac{n\pi}{L}(R - R_1)\right], \qquad E_n = \frac{n^2\pi^2\hbar^2}{2mL^2}, \tag{2.33}$$

where $L \coloneqq R_N - R_1$ represents the length of the box. In this method, the artificial boundary conditions are inherently incorporated by the choice of this basis.

In this method, we introduce a new numerical parameter N_{DVR}, which corresponds to the number of particle-in-a-box wavefunctions considered in the expansions; therefore, all the following matrices are $(N_{\mathrm{DVR}} \times N_{\mathrm{DVR}})$-dimensional. The implementation of this method consists of two steps. Firstly, we compute the matrix elements of the $\hat{R}$ operator on a grid shifted by $-C$, where $C \coloneqq (R_1 + R_N)/2$. If $R_1 = 0$, then $C = L/2$. This adjustment ensures

that the diagonal matrix elements are zero. For the matrix elements of the operator $\hat{R}$, the following relations hold:

$$\begin{aligned}\mathbb{R}: \quad R_{mn} &= \frac{2}{L}\int_{R_1-C}^{R_N-C} \sin\left[\frac{m\pi}{L}(R-R_1+C)\right] R \sin\left[\frac{n\pi}{L}(R-R_1+C)\right] \mathrm{d}R \\ &= \frac{-8Lmn}{\pi^2(m^2-n^2)^2} \qquad \text{for } m+n=1 \mod 2 \end{aligned} \tag{2.34}$$

After diagonalizing this matrix, we obtain matrix $\mathbb{A}$, whose columns are the eigenvectors of the operator $\hat{R}$. The diagonal matrix $\mathbb{D}$ of its eigenvalues is represented as $\mathbb{R} = \mathbb{A}\mathbb{D}\mathbb{A}^T$. The eigenvalues in $\mathbb{D}$ are then shifted back by $+C$.

The second step involves the construction of the Hamiltonian matrix $\mathbb{H} = \mathbb{T} + \mathbb{V}$. Here, the matrix $\mathbb{T}$, which represents the kinetic energy operator, is diagonal with the energy values of the corresponding particle-in-a-box energies on its diagonal, $(\mathbb{T})_n = E_n$ (2.33). The matrix $\mathbb{V}$, which accounts for the potential energy, is expressed as

$$\mathbb{V} = \mathbb{A}V(\mathbb{D})\mathbb{A}^T, \tag{2.35}$$

where $V(\mathbb{D})$ is the potential energy evaluated at the eigenvalues of the operator $\hat{R}$. From (2.28) we again derive an eigenvalue equation

$$\mathbb{H}\tilde{\boldsymbol{\psi}} = E\tilde{\boldsymbol{\psi}}, \tag{2.36}$$

where E corresponds to the eigenenergies of the system. However, this time the eigenvectors $\tilde{\boldsymbol{\psi}}$ are N_{DVR}-dimensional, and their elements are the coefficients for the sought vibrational wavefunctions in the φ_n basis. Consequently, we can calculate the k-th vibrational wavefunction at any $R \in (R_1, R_N)$ using the relation

$$\psi^{(k)}(R) = \sqrt{\frac{2}{L}} \sum_{n=1}^{N_{\mathrm{DVR}}} \tilde{\psi}_n^{(k)} \sin\left[\frac{n\pi}{L}(R-R_1)\right], \tag{2.37}$$

where $\tilde{\psi}_n^{(k)}$ are the components of the k-th eigenvector $\tilde{\boldsymbol{\psi}}^{(k)}$. The received eigenenergies $E^{(k)}$ require no further transformation. The number of vibrational wavefunctions calculated is N_{DVR}. In our implementation of the Four-DVR method, both diagonalizations were carried out using the DSYEV procedure from the LAPACK library [4].

2.2.2 Construction of the Green's operator

The next crucial step involves calculating the retarded Green's operator $\hat{G}^{(+)}$ with the appropriate boundary conditions, as outlined between equations

(2.3) and (2.4). It turns out to be more computationally efficient not to calculate the full Green's operator; but rather to implement a procedure that solves the non-homogeneous Schrödinger equation with the appropriate boundary conditions for its solution $\psi(R)$:

$$\left[E - \hat{H}_1\right] \psi(R) = \varphi(R), \tag{2.38}$$

where $\hat{H}_1 = \hat{T}_N + V_1(R)$, $\hat{T}_N$ represents the vibrational kinetic operator, and the right-hand side is given by $\varphi(R)$.

The appropriate boundary conditions for this equation are specified as follows

$$\psi(0) = 0, \qquad \frac{\psi'(R)}{\psi(R)} \propto ik. \tag{2.39}$$

These conditions ensure that the solution describes an outgoing wave, characterized by the wavenumber k defined by the relation $k \coloneqq \sqrt{2mE}/\hbar$. For negative energies, k is redefined as $k \coloneqq i\sqrt{2m|E|}/\hbar$, leading to an exponentially decaying wavefunction, which conforms to physical expectations.

To solve the equation (2.38), we begin by solving for the Green's function $G(R, R')$

$$\left[E - \hat{T}_N - V_1(R)\right] G(R, R') = \delta(R - R'), \tag{2.40}$$

where δ is the Dirac delta distribution. This equation, along with the required boundary conditions, can be addressed by first tackling the homogeneous equation

$$\left[E - \hat{T}_N - V_1(R)\right] \psi_{\mathrm{R/I}}(R) = 0, \tag{2.41}$$

where the regular solution $\psi_{\mathrm{R}}(R)$ satisfies the condition $\psi_{\mathrm{R}}(0) = 0$, and the irregular solution $\psi_{\mathrm{I}}(R)$ meets the criteria for an outgoing wave at $R \to \infty$. It can be easily verified that the following combination of these two solutions satisfies equation (2.40) while simultaneously meeting both boundary conditions (2.39)

$$G(R, R') = \begin{cases} \frac{2m}{\hbar^2} \frac{\psi_{\mathrm{I}}(R')}{W(R')} \psi_{\mathrm{R}}(R) & \text{for } R < R' \\ \frac{2m}{\hbar^2} \frac{\psi_{\mathrm{R}}(R')}{W(R')} \psi_{\mathrm{I}}(R) & \text{for } R > R', \end{cases} \tag{2.42}$$

where $W(R')$ is the Wronskian determinant defined as

$$W(R') = \psi_{\mathrm{R}}(R')\psi'_{\mathrm{I}}(R') - \psi'_{\mathrm{R}}(R')\psi_{\mathrm{I}}(R'), \tag{2.43}$$

and due to the nature of the differential equation (2.41), $W(R')$ is constant across all R' (as derived from [8]), allowing its computation at just one specific R'.

To calculate the regular and irregular solutions $\psi_{\mathrm{R/I}}$ of the equation (2.41) on the grid $\boldsymbol{R}$ (see (2.25)), we can use the *Numerov method* which utilizes the discretization of the second derivative in (2.41). Using [9], we can derive the following relationship between the values of $\psi_{\mathrm{R/I}}$ at adjacent points on $\boldsymbol{R}$

$$\left[1+\tfrac{(\Delta R)^2}{12}\mathcal{E}_{j+1}\right]\psi_{j+1}-2\left[1-\tfrac{5(\Delta R)^2}{12}\mathcal{E}_j\right]\psi_j+\left[1+\tfrac{(\Delta R)^2}{12}\mathcal{E}_{j-1}\right]\psi_{j-1}\approx 0 \quad (2.44)$$

where $\psi_k=\psi_{\mathrm{R/I}}(R_k)$ and $\mathcal{E}_k \coloneqq \frac{2m}{\hbar^2}\left[E-V_1(R_k)\right]$. We can then calculate the regular solution ψ_{R} by setting the boundary condition at R_1 and R_2, and then propagate $\psi_{\mathrm{R}}(R_k)$ for $k\in\{3,4,\cdots,N\}$ using (2.44). Similarly, the irregular solution ψ_{I} is obtained by applying the boundary condition at R_N and R_{N-1}, and subsequently propagating $\psi_{\mathrm{I}}(R_k)$ backwards for $k\in\{N-2,N-3,\cdots,1\}$. The corresponding boundary condition for the regular solution is

$$\psi_{\mathrm{R}}(R_1)=0 \qquad \text{and} \qquad \psi_{\mathrm{R}}(R_2)=\Delta R, \quad (2.45)$$

where the condition $\psi_{\mathrm{R}}(R_2)$ is actually arbitrary, as it merely sets the normalization of ψ_{R}, which does not affect the Green's function $G(R,R')$ (2.42). For numerical safety and to prevent excessively large function values, we choose ΔR. In a similar manner, the boundary condition for ψ_{I} is arbitrary and using any two values whose discretized derivative corresponds to an outgoing wave (2.39) is possible. For simplicity, we choose

$$\psi_{\mathrm{I}}(R_N)=e^{ikR_N} \qquad \text{and} \qquad \psi_{\mathrm{I}}(R_{N-1})=e^{ikR_{N-1}}. \quad (2.46)$$

After obtaining the regular and irregular solutions $\psi_{\mathrm{R/I}}$, we need to compute the Wronskian determinant $W(R')$ (2.43). This is achieved by using a discretization formula for the necessary derivatives of both solutions. In our case, we utilized a discretization formula with the same order of error as the *Numerov method* [9]. However, a higher-order formula could be used without significantly increasing computational demand, as the Wronskian needs to be calculated at just one specific R', as previously discussed. The utilized higher-order central difference formula for the derivatives is [5]

$$\psi'_j\approx\frac{-\psi_{j+3}+9\psi_{j+2}-45\psi_{j+1}+45\psi_{j-1}-9\psi_{j-2}+\psi_{j-3}}{60\Delta R}, \quad (2.47)$$

where $j\in\{4,\cdots,N-3\}$ is chosen to avoid edge effects and ensure accurate derivative estimates across the domain.

Now we have all the elements necessary to derive the final solution of (2.38) with the boundary condition (2.39) using the formula:

$$\begin{aligned}\psi(R)=\int G(R,R')\varphi(R')\,\mathrm{d}R' = \frac{2m}{\hbar^2 W}\Bigg[&\psi_{\mathrm{I}}(R)\int_{R_1}^{R}\psi_{\mathrm{R}}(R')\varphi(R')\,\mathrm{d}R' \\ &+\psi_{\mathrm{R}}(R)\int_{R}^{R_N}\psi_{\mathrm{I}}(R')\varphi(R')\,\mathrm{d}R'\Bigg],\end{aligned} \quad (2.48)$$

where we have used the constancy of the Wronskian determinant $W(R') \equiv W$. The calculation for $\psi(R)$ can be optimized by first computing the 'primitive functions' $\Psi_{\mathrm{R/I}}(R)$ at all R in $\boldsymbol{R}$:

$$\Psi_{\mathrm{R}}(R) \coloneqq \int_{R_1}^{R} \psi_{\mathrm{R}}(R')\varphi(R')\,\mathrm{d}R', \quad \Psi_{\mathrm{I}}(R) \coloneqq \int_{R}^{R_N} \psi_{\mathrm{I}}(R')\varphi(R')\,\mathrm{d}R' \tag{2.49}$$

This can be achieved by successively applying the trapezoidal rule (2.27) on each interval (R_k, R_{k+1}) for all points in $\boldsymbol{R}$, which results in the recursive formulae:

$$\Psi_{\mathrm{R}}(R_{k+1}) = \Psi_{\mathrm{R}}(R_k) + \frac{\Delta R}{2}\left[\psi_{\mathrm{R}}(R_k)\varphi(R_k) + \psi_{\mathrm{R}}(R_{k+1})\varphi(R_{k+1})\right], \tag{2.50}$$

$$\Psi_{\mathrm{I}}(R_{k-1}) = \Psi_{\mathrm{I}}(R_k) + \frac{\Delta R}{2}\left[\psi_{\mathrm{I}}(R_k)\varphi(R_k) + \psi_{\mathrm{I}}(R_{k-1})\varphi(R_{k-1})\right], \tag{2.51}$$

where $\Psi_{\mathrm{R}}(R_1) = \Psi_{\mathrm{I}}(R_N) = 0$. Ultimately, using the computed 'primitive functions' $\Psi_{\mathrm{R/I}}(R)$, we obtain the final formula for the sought solution ψ on the grid $\boldsymbol{R}$:

$$\psi(R_j) = \frac{2m}{\hbar^2 W}\left[\psi_{\mathrm{I}}(R_j)\Psi_{\mathrm{R}}(R_j) + \psi_{\mathrm{R}}(R_j)\Psi_{\mathrm{I}}(R_j)\right] \tag{2.52}$$

2.2.3 F and M operators

The final step involves calculating the integral transforms $\mathcal{F}(\varepsilon)$ (2.6) for the non-local level-shift operator $\hat{F}$ and $\mathcal{M}(\varepsilon)$ (2.22) for the $\hat{M}$ operator. Utilizing the identity for the integral transform, derived in [10], we express

$$\mathcal{F}(\varepsilon) = \int_0^\infty \frac{f^2(\epsilon)}{\varepsilon - \epsilon + i\eta}\,\mathrm{d}\epsilon = \text{p.v.}\int_0^\infty \frac{f^2(\epsilon)}{\varepsilon - \epsilon}\,\mathrm{d}\epsilon - i\pi f^2(\varepsilon). \tag{2.53}$$

This identity, formulated for $\mathcal{F}(\varepsilon)$, similarly applies to $\mathcal{M}(\varepsilon)$.

The formula (2.53) can be, in principle, used to calculate the integral transforms $\mathcal{F}(\varepsilon)$ and $\mathcal{M}(\varepsilon)$ for general functions $f(\epsilon)$ and $f_\mu(\epsilon)$. However, the presence of the principal value integral requires careful numerical treatment, and the trapezoidal rule (2.27) cannot simply be used, as, for example, for each different ε, a unique grid in ϵ would have to be chosen which is symmetrical around ε. The fact that this integral has an unbounded upper limit poses another, yet more easily solvable problem. In this thesis, however, we assume a special form of functions $f(\epsilon)$ and $f_\mu(\epsilon)$

$$\gamma(\epsilon) \coloneqq 2\pi f^2(\epsilon) = A_\gamma \left[\tfrac{\epsilon}{B_\gamma}\right]^\alpha \exp\left[-\tfrac{\epsilon}{B_\gamma}\right], \tag{2.54}$$

$$\gamma_\mu(\epsilon) \coloneqq 2\pi f_\mu^2(\epsilon) = A_\mu \left[\tfrac{\epsilon}{B_\mu}\right]^\alpha \exp\left[-\tfrac{\epsilon}{B_\mu}\right], \tag{2.55}$$

where A_γ, B_γ, A_μ, B_μ, and α are constants specific to the chosen molecular model, as detailed in Appendix A. This allows us to compute the principal value integral in (2.53) analytically using a formula derived from [11]

$$\text{p.v.} \int_0^\infty \frac{x^\alpha e^{-\beta x}}{\varepsilon - x}\, \mathrm{d}x = \begin{cases} -\Gamma(1+\alpha)|\varepsilon|^\alpha \Gamma(-\alpha; \beta|\varepsilon|) e^{-\beta\varepsilon} & \varepsilon < 0, \\ \varepsilon^\alpha e^{-\beta\varepsilon} \left[\pi \cot(\alpha\pi) - \Gamma(\alpha)(\beta\varepsilon)^{-\alpha} \right. & \\ \qquad \left. - {}_1F_1(-\alpha, 1-\alpha; \beta\varepsilon)\right] & \varepsilon > 0, \end{cases} \tag{2.56}$$

where $\Gamma(a)$ is the gamma function, $\Gamma(a;x)$ is the upper incomplete gamma function, and ${}_1F_1(a,b;x)$ is the confluent hypergeometric function.

The gamma function $\Gamma(a)$ is directly implemented in FORTRAN 90. The upper incomplete gamma function $\Gamma(a;x)$ can be calculated using the following continued fraction approach, detailed in [11]

$$\Gamma(a;x) = x^\alpha e^{-x} \left[\frac{1}{x+} \frac{1-\alpha}{1+} \frac{1}{x+} \frac{2-\alpha}{1+} \frac{2}{x+} \cdots \right]. \tag{2.57}$$

To evaluate the confluent hypergeometric function, a series expansion method can be utilized, also discussed in [11]

$${}_1F_1(a,b;x) = 1 + \frac{a}{b}\, x + \frac{a(a+1)}{b(b+1)} \frac{x^2}{2!} + \frac{a(a+1)(a+2)}{b(b+1)(b+2)} \frac{x^3}{3!} + \cdots . \tag{2.58}$$

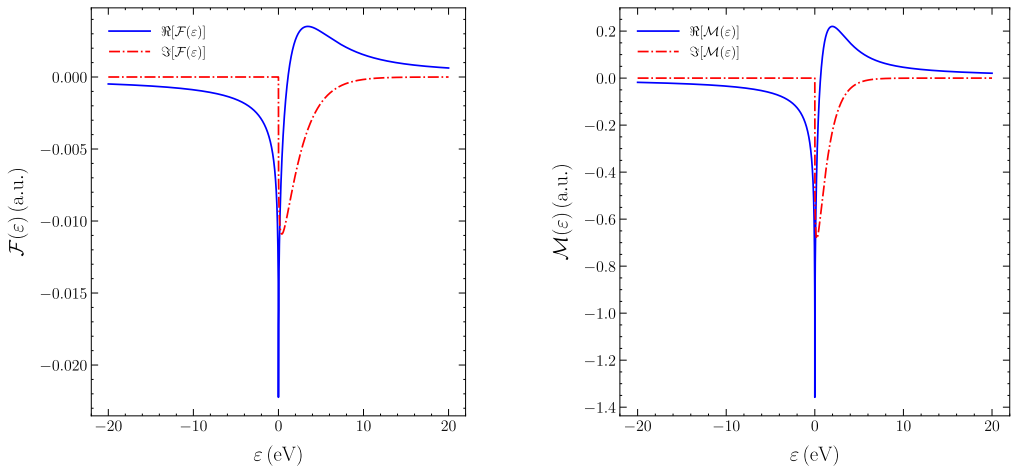

Figure 2.1 Energetic profiles of the integral transforms $\mathcal{F}(\varepsilon)$ (left) and $\mathcal{M}(\varepsilon)$ (right) for the LiH model, as detailed in Appendix A.

2.2.4 Fixed-nuclei approximation

The numerical implementation of the fixed-nuclei approximation is now straightforward. With the integral transforms $\mathcal{M}(\varepsilon)$ and $\mathcal{F}(\varepsilon)$ at hand (see 2.2.3), we can evaluate the moment function $\mu(R;\varepsilon_\gamma)$ (1.41) for all nuclear separations R and any energy ε_γ of the incoming photon using the conservation of energy relation (1.35).

To further calculate the fixed-nuclei amplitudes, we first determine the eigenstates in the potentials $W(R)$ and $V_0(R)$ (as discussed in 2.2.1). Subsequently, we integrate the moment function $\mu(R;\varepsilon_\gamma)$ over all R using the derived eigenstate wavefunctions as a weighting function. This integration is performed utilizing the trapezoidal rule (2.27).

2.3 Testing of convergence

In the previous section, several numerical parameters were introduced for our calculations, namely:

- R_N – the length of the grid (2.25),
- N – the number of grid points (2.25),
- N_{DVR} – the number of particle-in-a-box wavefunctions used in the Four-DVR method (2.37),
- n_κ – this parameter, which has not been explicitly mentioned before, represents the number of states $\langle\nu|\hat{g}$ onto which the equation (2.9) was projected, and also the number of eigenstates $|\nu\rangle$ of $\hat{h}_0$ used in the expansion of the operators $\hat{F}$ and $\hat{M}$ (2.7). Therefore, it also determines the dimension of matrices $\mathbb{G}$, $\mathbb{F}$ and vectors $\boldsymbol{p}$, $\boldsymbol{r}$ in the main equation (2.11).

The precise numerical values of these parameters must be carefully selected to ensure that the results remain stable under small perturbations of these parameters, while allowing for more substantial adjustments, such as increasing the number of grid points, which should ideally lead to improved accuracy without disproportionately affecting the final results. This confirms that the results are numerically converged. Testing these parameters is intricate due to their interdependencies.

2.3.1 Bound eigenstates

In Section 2.2.1, we outlined two methods for calculating eigenstates within a given potential: grid discretization and the Four-DVR method. The accuracy of these methods depends on the parameters N and N_{DVR} respectively. To ensure accurate energy calculations for bound states, it is crucial that the potential becomes constant near R_N.

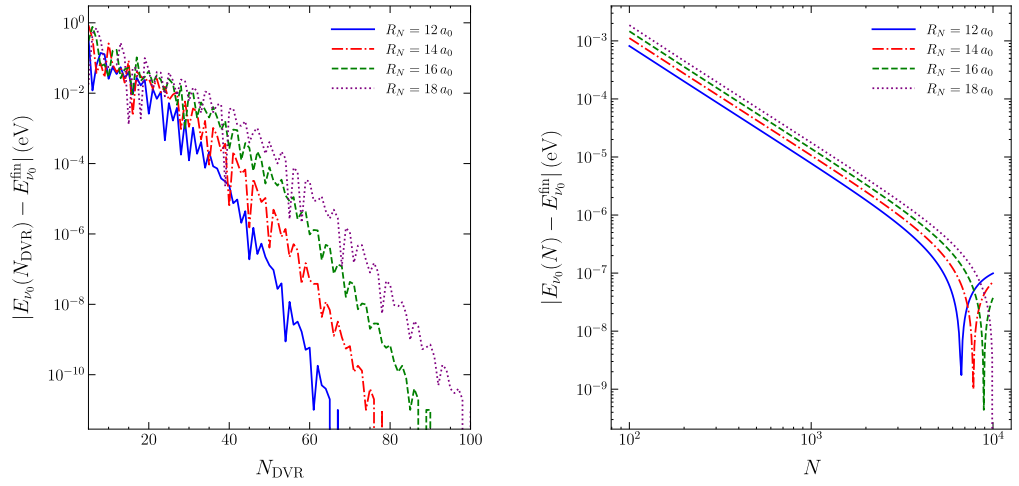

(a) Four-DVR method – $W(R)$ **(b)** Grid discretization – $W(R)$

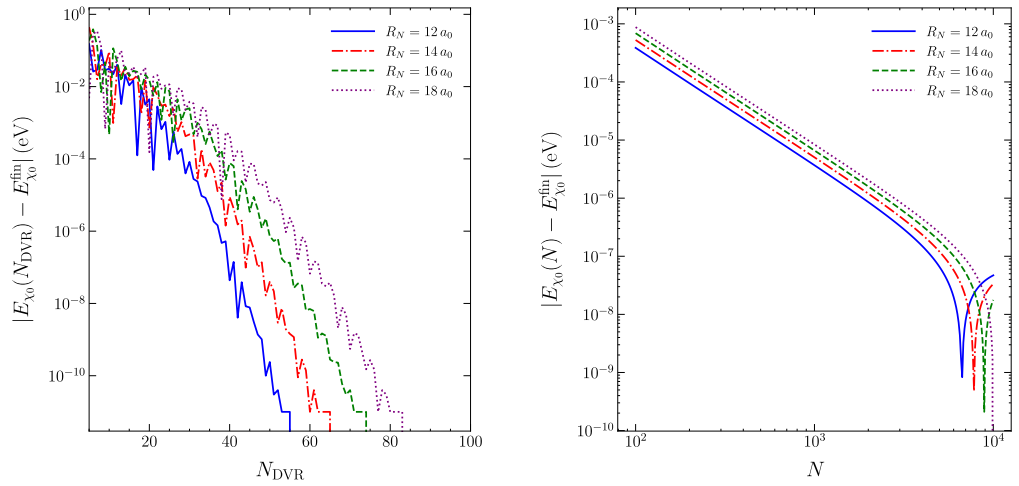

(c) Four-DVR method – $V_0(R)$ **(d)** Grid discretization – $V_0(R)$

Figure 2.2 Convergence tests for the ground state energy calculations for different potentials corresponding to the LiH model (see Appendix A).

Our molecular models (see Appendix A) utilize Morse potentials. Typically, the convergence of bound state calculations can be assessed by comparing numerically obtained energies E_i with the analytically computed energies for the bound states in the Morse potential (derived in [12]). However, our boundary condition for a zero wave function at $R = 0$ differs from the analytical solution, which assumes $R \in (-\infty, \infty)$. Therefore, the analytical energies only approximate our problem. For convergence analysis, we compare with the energy E_i^{fin} obtained for the largest N or N_{DVR} and the largest R_N. While this value might be considered in some respects as the most precise due to maximizing computational parameters, it may not truly be the most accurate due to potential cumulative rounding errors. Thus, this comparison should be approached with caution. Here, we present a convergence test for the ground state energy, as illustrated in Fig. 2.2.

From Fig. 2.2, it is evident that the Four-DVR method achieves better precision than the grid discretization method with a significantly lower number of elements, making it computationally more efficient. Additionally, the Four-DVR method allows for the computation of corresponding eigenfunctions on any desired grid with any required accuracy, which is not feasible using the grid discretization method. Therefore, we exclusively utilize the Four-DVR method for subsequent calculations.

Furthermore, Fig. 2.2 demonstrates that the ground state energy, when sufficiently converged with respect to N or N_{DVR}, does not depend on the choice of R_N for $R_N > 12\,a_0$. Thus, $R_N = 12\,a_0$ is considered sufficient for achieving convergence in bound state calculations of the LiH model. We also observe that convergence is fastest for the smallest R_N. This can be explained by the higher oscillations in the basis functions for smaller R_N in the Four-DVR method, which are better at describing a wavefunction localized at the bottom of the potential. A similar explanation applies to the grid discretization method, where higher resolution is achieved with a smaller R_N for the same number of grid points N.

2.3.2 Discretized continuum

In the previous subsection, we primarily discussed the convergence and accuracy of the bound spectrum of $\hat{h}_0$. However, the unbound part, mentioned briefly in Section 2.2, is equally important. Our numerical methods artificially discretize this continuous spectrum due to inherent computational limitations. This discretization directly ties to the choice of n_κ, the number of states considered in our computations.

Due to computational limits, we can only consider a finite number of states $|\nu\rangle$. Fortunately, the contribution of higher states $|\nu\rangle$ diminishes as

the arguments of integral transforms $\mathcal{F}(E - E_\nu)$ and $\mathcal{M}(E - E_\nu)$ approach large negative values for $E_\nu \gg E$. As illustrated in Fig. 2.1, the real part of integral transforms significantly decreases for large negative arguments and their imaginary part is trivially equal to zero, justifying the neglect of contributions from states $|\nu_j\rangle$ for $j > n_\kappa$ within the studied energy range corresponding to the total conserving energy E.

Moreover, the described energy range is not the only important factor, as the density of the discretization is also crucial. As observed from Fig. 2.1, the integral transforms $\mathcal{F}(\varepsilon)$ and $\mathcal{M}(\varepsilon)$ contribute significantly when their argument approaches zero. If the discretization is too sparse, the final results show noticeable artifacts of this discretization, characterized by a non-smooth behavior with sharp spikes. A denser grid helps mitigate these artifacts.

For energies large enough such that $E_{\nu_n} \gg W$, the energies of the discretized continuum behave similarly to the particle-in-a-box spectrum, following the relation [7]

$$E_{\nu_n} \approx \frac{n^2\pi^2\hbar^2}{2mL^2}. \tag{2.59}$$

From this equation, we observe that the choice of R_N plays a role in another aspect of the numerical convergence of our results. Firstly, a higher value of R_N leads to a denser discretization. Furthermore, with a constant n_κ, a higher R_N leads to lower maximal energy. Therefore, if we increase R_N we need to proportionally increase n_κ to keep the maximal described energy constant.

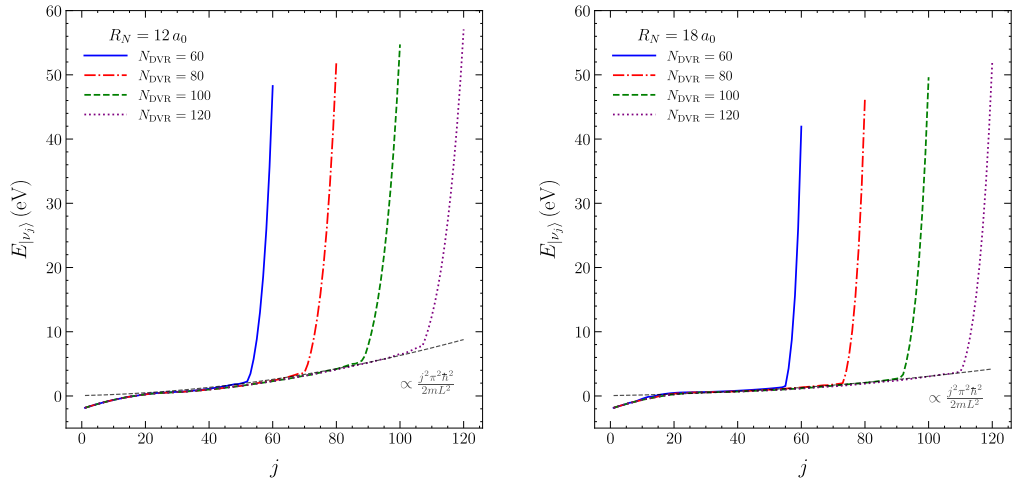

Figure 2.3 Dependency of energy E_{ν_j} on the state $|\nu_j\rangle$ in the potential $W(R)$ of the LiH model (see Appendix A) for different N_{DVR} and R_N settings.

Another non-trivial relation exists between n_κ and N_{DVR}. To obtain at least n_κ states $|\nu\rangle$, we need $N_{\mathrm{DVR}} \geq n_\kappa$. As illustrated in Fig. 2.3, for $j \ll N_{\mathrm{DVR}}$ the unbound energies E_j follow the relation (2.59); however, as j approaches N_{DVR}, the energy difference between consecutive states suddenly increases rapidly. This phenomenon is caused by the cut-off in the calculated eigenstates. From this, we deduce that n_κ can be safely varied within ranges that are sufficiently distant from N_{DVR}. The difference in energy density for different R_N values can also be observed by comparing the images in Fig. 2.3.

2.3.3 'Tail' implementation for the Green's operator

Previously, we have demonstrated the advantages of selecting a smaller R_N, where the boundary condition for the zero wavefunction of bound states is adequately satisfied. However, it is possible to encounter a case where the bound states in potentials V_0 and W are converged with respect to R_N, while simultaneously, the potential $V_1(R)$ is not close enough to zero at R_N. Therefore, the enforced boundary condition for the outgoing wave (2.46) on the irregular solution ψ_{I} during the construction of the Green's operator $\hat{G}^{(+)}$ will not be accurate. The resulting behavior of the wavefunction will resemble an instance where the wavefunction reflects off a sharp potential edge. This can be demonstrated using the simplest application of the Green's operator $\hat{G}^{(+)}$, namely the scattered wavefunction for the vibrational excitation process in the *First Born approximation*

$$|\psi_1\rangle = \hat{G}^{(+)} V_{1\epsilon_i} |\nu_i\rangle = f(\epsilon_i) \hat{G}^{(+)} \hat{g} |\nu_i\rangle. \tag{2.60}$$

This phenomenon is illustrated in Fig. 2.4a. Here, we clearly see that the absolute value of the wavefunction oscillates, which corresponds to a situation where the wavefunction is not perfectly outgoing but has been partially reflected at the sharp edge of the potential.

Luckily, we can easily correct the inaccurate boundary condition by implementing a 'tail' described by a numerical parameter t during the construction of the Green's operator $\hat{G}^{(+)}$. Essentially, this means that we create a new, longer grid $\boldsymbol{R}'$ with tN number of points and final point $R'_{tN} = tR_N$, thereby extending the original grid to t-times its length while maintaining the step size. Now, we can set the boundary condition for the irregular solution ψ_{I} at the end of this grid

$$\psi_{\mathrm{I}}(R'_{tN}) = e^{ikR'_{tN}} \quad \text{and} \quad \psi_{\mathrm{I}}(R'_{tN-1}) = e^{ikR'_{tN-1}}, \tag{2.61}$$

where the potential V_1 is safely close enough to zero. Afterward, we propagate the irregular solution backwards using the same procedure as in Section 2.2.2.

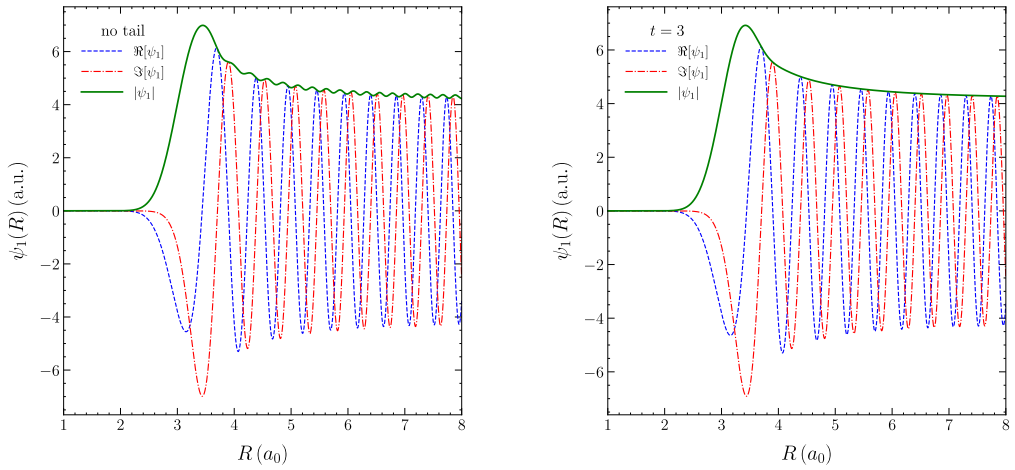

(a) No tail implemented

(b) Tail implemented with $t = 3$

Figure 2.4 Comparison of scattered wavefunctions for vibrational excitation in the first Born approximation, illustrating the effects of tail implementation.

Because we assume that the wavefunctions we apply the Green's operator on are zero outside the original grid $\boldsymbol{R}$, it suffices to consider only the part of the irregular solution on the grid $\boldsymbol{R}$, where this segment has already undergone propagation with the adjusted boundary condition. The fact that the final wavefunction has the correct boundary condition, corresponding to an outgoing wave, can be seen in Fig. 2.4b.

2.3.4 Convergence of the results

In the final stages of our analysis, we need to ensure that the results for the photodetachment amplitudes and vibrational excitation amplitudes are converged with respect to the numerical parameters previously discussed, over the studied energy range. This convergence testing involves initially identifying a set of numerical parameters assumed to yield converged results. Subsequently, we increase these parameters as their elevation corresponds to a reduction in the neglect of certain aspects of the problem. While doing so, we respect the interdependencies between these parameters mentioned in earlier sections. Then, all amplitudes are recalculated and compared with the previous calculations to derive the following metrics: the average relative deviation $\overline{\eta}$ and the maximum relative deviation $\eta^{\max}$, defined for an

amplitude $A_\bullet$ by the relation

$$\eta(\varepsilon) = \frac{|A_\bullet^{(j)}(\varepsilon) - A_\bullet^{(j+1)}(\varepsilon)|}{A_\bullet^{(j)}(\varepsilon)} \tag{2.62}$$

where the average and maximum are taken over the studied energy interval ε. If these relative deviations reach values within the desired accuracy, we consider the results to be converged.

Tables describing the convergence of individual results are provided in Appendix B for different molecular models (see Appendix A). It is important to note that the convergence parameters may vary significantly across models, necessitating separate convergence analyses for each model.

Chapter 3

Discussion of results

In this chapter, we present our findings on the numerically calculated amplitudes for photodetachment, specifically focusing on the LiH model. We explore the physical interpretation of each component within the photodetachment amplitude and draw comparisons with the vibrational excitation process, for which amplitudes were also computed. We continue our analysis by examining the photodetachment amplitudes obtained using the fixed-nuclei approximation and compare their accuracy and precision with those calculated using full dynamics for the LiH model. Additionally, we will introduce the N_2 model and discuss the phenomenon known as Boomerang oscillations associated with it.

3.1 Photodetachment amplitude

In this section, we discuss the results shown in Fig. 3.1, which illustrates the dependence of the numerically calculated photodetachment amplitude, with the final vibrational state being the ground state $|\nu_0\rangle$ of the neutral molecule, on the energy of the incoming photon ε_γ. Alongside the total amplitude A, we also present individual components of the photodetachment amplitude, namely: the direct amplitude A_{dir}, the resonant amplitude A_{res}, and the attachment amplitude A_{att}. These components correspond to different physical processes, detailed in Section 1.5 through equations (1.32), (1.33), and (1.34). For clarity, it should be noted that the square of the total amplitude $|A|^2$ is not simply the sum of the squares of these contributing amplitudes due to their non-trivial phase relationships.

From Fig. 3.1, we observe that the contributions from the resonant and the attachment processes are similar. They are particularly significant around an incoming photon energy of $\varepsilon_\gamma \approx 4\,\text{eV}$. This energy corresponds to the

resonance energy, which is effectively the energy difference between the anion ground state E_{χ_0} and the energy of the discrete-state-in-continuum described by the potential curve $V_1(R)$, specifically at a value of R near where the anion ground state is primarily localized. This can be seen in Fig. A.1, which illustrates the LiH molecular model.

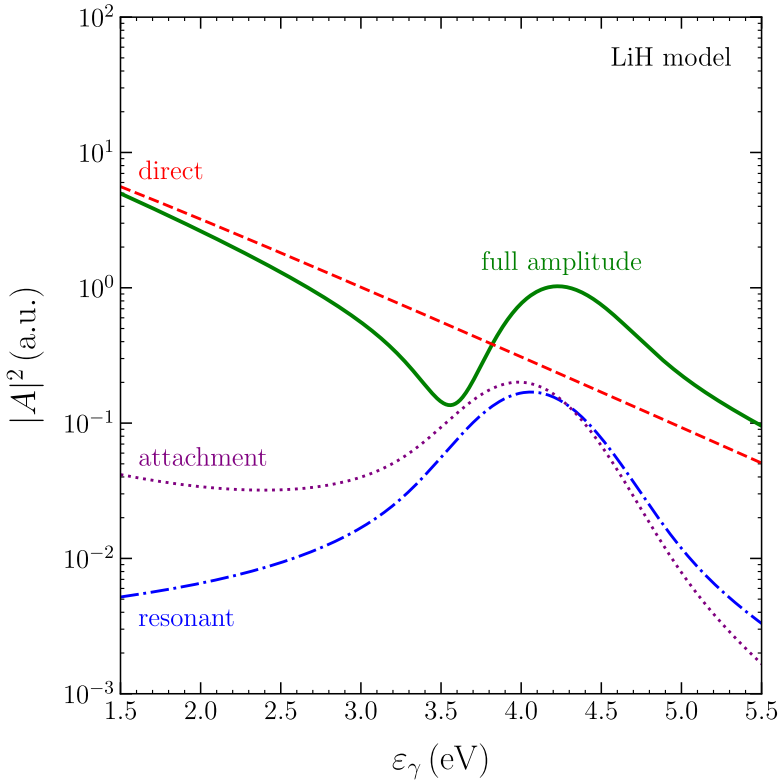

Figure 3.1 Energy dependence of the squared photodetachment amplitude $|A|^2$ for the LiH model, where the final vibrational state is the ground state $|\nu_0\rangle$ of the neutral molecule. The graph illustrates contributions from different components of the photodetachment process: direct (A_{dir}), resonant (A_{res}), and attachment (A_{att}), alongside the full amplitude.

3.2 Decline for higher vibrational states

We now turn our attention to the decline in amplitude for higher vibrational states within the photodetachment process. This section examines how the amplitude of photodetachment transitions decreases when the final states

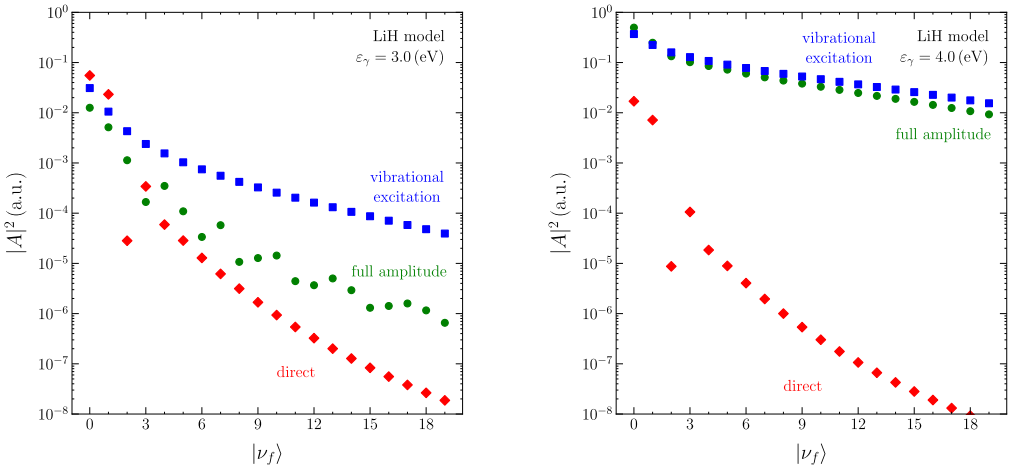

Figure 3.2 Dependence of the photodetachment amplitude for the LiH model on the final vibrational state of the neutral molecule $|\nu_f\rangle$, shown for two different incoming electron energies ε_γ. For comparison, the amplitudes of the direct component of photodetachment and the vibrational excitation cross-sections by electron scattering, using the same energy as the incoming photon, are also plotted.

are higher vibrational states of the neutral molecule. Fig. 3.2 illustrates the dependence of the square of the full photodetachment amplitude $|A|^2$ on the final vibrational state. For comparative purposes, we also include values of the direct photodetachment amplitude and the vibrational excitation cross-sections of the neutral molecule by electron scattering.

From the graphs in Fig. 3.2, calculated for two distinct incoming photon energies; or incoming electron energies for vibrational excitation; it is observed that for the energy $\varepsilon_\gamma = 3\,\mathrm{eV}$, which is well below the resonance maximum, the full photodetachment amplitude rapidly decreases with higher final vibrational states. However, this decrease is significantly mitigated at the incoming electron energy of $\varepsilon_\gamma = 4\,\mathrm{eV}$, corresponding to the resonance energy. The direct component diminishes similarly at both energies, reflecting that in our model, the direct component is largely influenced by the overlap between the ground vibrational state of the anion $|\chi_0\rangle$ and the final vibrational states of the neutral molecule $|\nu_f\rangle$, which declines rapidly for higher vibrational states.

Furthermore, Fig. 3.2 reveals that at the resonance energy, the full photodetachment amplitude is comparable in magnitude to the cross-section of vibrational excitation by electron scattering at the same energy as the incoming electron. Additionally, from both graphs in Fig. 3.2 and those in Fig. 3.3, it can be concluded that for higher final vibrational states, the resonant and attachment processes dominate over the direct component.

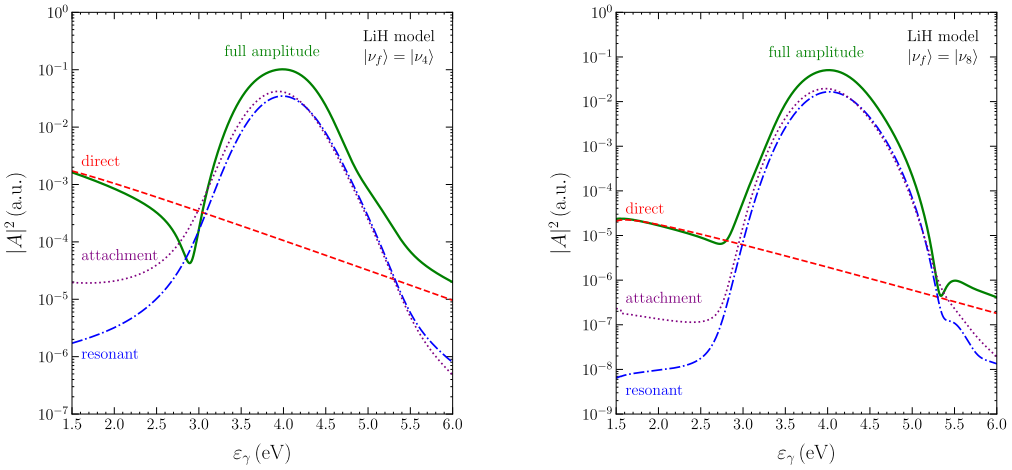

Figure 3.3 Energy dependence of the squared photodetachment amplitude $|A|^2$ for the LiH model, shown for the fourth $|\nu_4\rangle$ (left) and eighth $|\nu_8\rangle$ (right) vibrational states of the neutral molecule as final states. The graphs also illustrates contributions from different components of the photodetachment process

3.3 Fixed-nuclei approximation

This section is dedicated to the discussion of the fixed-nuclei approximation, which was extensively described in Section 1.6. In Figure 3.4, we present the full photodetachment amplitude calculated using the fixed-nuclei approximation, denoted as A_{FN} and governed by Equation (1.42). Additionally, the integral fixed-nuclei approximation amplitude for photodetachment, $A_{\mathrm{FN}}^{(\mathrm{int})}$, defined by Equation (1.43), is also depicted. To evaluate the precision of this approximation, the full photodetachment amplitude A, computed using the complete dynamics, is included for comparison. The comparative analysis allows us to determine that the fixed-nuclei approximation provides qualitatively similar results for the LiH model, although its limitations are evident. For a detailed and precise comparison, the resonant and attachment components of the amplitude for both the complete dynamics and fixed-nuclei calculations are separately illustrated in Figure 3.5. The direct component is omitted from this comparison as it remains invariant across both computational approaches, reflecting no dynamic influence.

Additionally, both Fig. 3.4 and 3.5 include plots of the fixed-R moment function $\mu(R)$, along with its components, for various values of R. Compared to the photodetachment amplitudes, the peaks of the moment function are significantly narrower. The incoming electron energy ε_γ, corresponding to these peaks, i. e. the resonance energy, precisely matches the energy difference

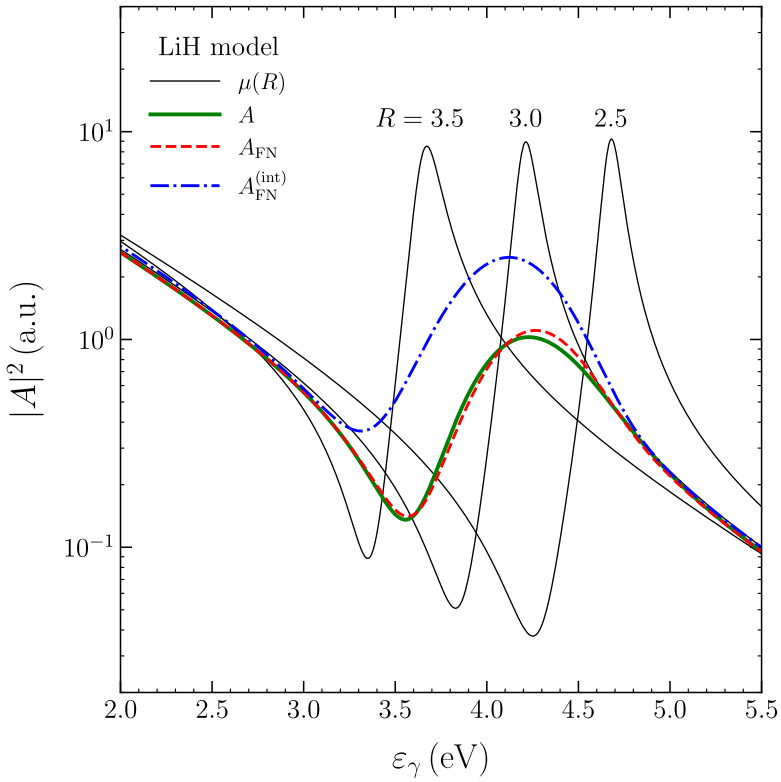

Figure 3.4 Energy dependence of the squared photodetachment amplitude $|A|^2$ for the LiH model, comparing amplitude computed with full dynamics with fixed-nuclei approximation and integral fixed-nuclei approximation amplitude. Additionally, the graph includes values of the fixed-R moment function μ for various R values, provided in Bohrs.

between the potential curves $V_0(R)$ and $V_1(R)$ at the respective R values. Figures 3.4 and 3.5 suggest that the final photodetachment amplitude results from the broadening of the fixed-R moment functions across the distribution of nuclei at different R values, as determined by the initial vibrational wavefunction $\chi_0(R)$ and the final vibrational wavefunction $\nu_0(R)$. This is further evidenced by the fact that the resonance peak of the full photodetachment amplitude is closest to the peak of the fixed-R moment function $\mu(R)$ at $R = 3.0\,a_0$, approximately the bottom of the potentials V_0 and W, where the vibrational wavefunctions are most localized.

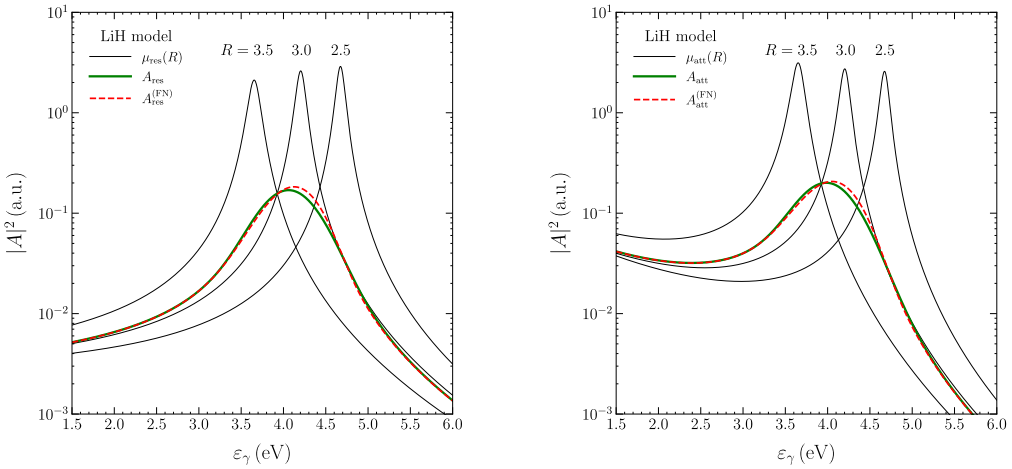

(a) resonant **(b)** attachment

Figure 3.5 Energy dependence of the resonant and attachment components of the photodetachment amplitude for the LiH model, comparing full-dynamics calculations with the fixed-nuclei approximation. The graphs also display values of the fixed-R moment function μ for various R values, provided in Bohrs.

3.4 Boomerang oscillations

In this section, we extend the application of our developed numerical methods to a new molecular model inspired by the N_2 molecule. This model, detailed in Appendix A, features significantly narrower and deeper potential wells compared to the LiH model previously discussed, presenting a new regime for testing our numerical approaches. Additionally, the energy range studied here is substantially below the dissociative attachment threshold, which differs from the conditions explored with the LiH model.

It should be noted that the N_2 molecule, in reality, does not possess a suitable low-lying anion state described by the potential V_0. Consequently, the N_2-inspired model utilizes realistic potentials $W(R)$ and $V_1(R)$, while the potential $V_0(R)$ is entirely fabricated. We have also devised the transition dipole elements, borrowing them from the LiH model. This approach is motivated by the desire to study mechanisms in the photodetachment physics rather than specific molecular characteristics.

The motivation for exploring the N_2-inspired model is to investigate whether the phenomenon known as *Boomerang oscillations*; observed in vibrational excitation by electron scattering cross-sections; has its analog in the photodetachment process. Boomerang oscillations refer to the energy variations in the energy phase of the nuclear wave function, reflecting within

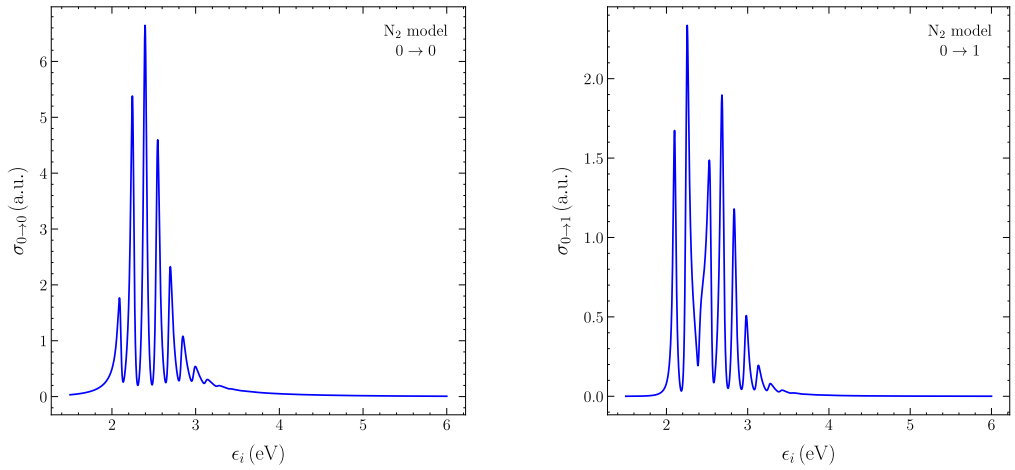

Figure 3.6 Energy dependence of the vibrational excitation of the neutral molecule by electron scattering cross-section for the N_2 model depicting the boomerang oscillations for two different final vibrational states.

the potential well of the molecular anion, a process documented in studies such as [2]. Additionally, having developed numerical methods to calculate

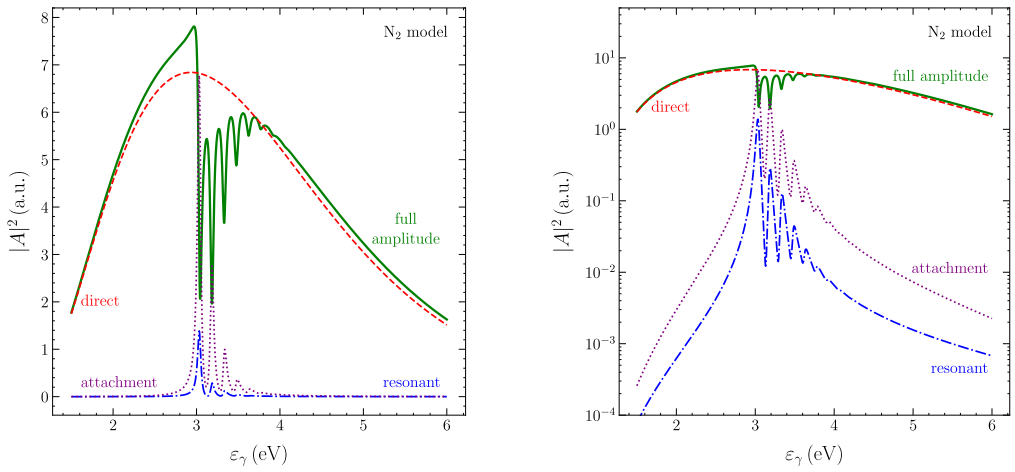

Figure 3.7 Energy dependence of the squared photodetachment amplitude $|A|^2$ for the N_2 model, where the final vibrational state is the ground state $|\nu_0\rangle$ of the neutral molecule. The graph illustrates contributions from different components of the photodetachment process: direct (A_{dir}), resonant (A_{res}), and attachment (A_{att}), alongside the full amplitude. The data is presented in both standard (left) and logarithmic (right) scales.

vibrational excitation cross-sections, we present our findings for the N_2 model in Fig. 3.6. Our results qualitatively match those described in [2] for the N_2 model.

On Fig. 3.7, we present the numerically calculated photodetachment amplitudes for the N_2 model, with the ground vibrational state of the neutral molecule as the final state. The individual components of the photodetachment amplitude are also depicted. From this figure, it becomes apparent that a phenomenon analogous to boomerang oscillations exists in the photodetachment process. This is particularly evident in the energy dependencies of the attachment and resonant components, which are more apparent in the logarithmic scale and display qualitative similarities to the vibrational excitation cross-sections.

Furthermore, the attachment and resonant components exhibit similar patterns but differ in magnitude, similar to observations made for the LiH model. These boomerang-like oscillations in the photodetachment process manifest within the full amplitude by modulating the dominant direct component.

Similarly to the LiH model, Fig. 3.7 shows that the first significant spike in photodetachment amplitude occurs at an incoming electron energy of approximately $\varepsilon_\gamma \approx 3\,\mathrm{eV}$. This resonance energy, which corresponds to the energy difference between the bottoms of the potential wells $V_0(R)$ and $V_1(R)$, can be visually confirmed in Fig. A.2, illustrating the N_2 molecular model.

In addition, Fig. 3.8 shows a comparison between the full photodetachment

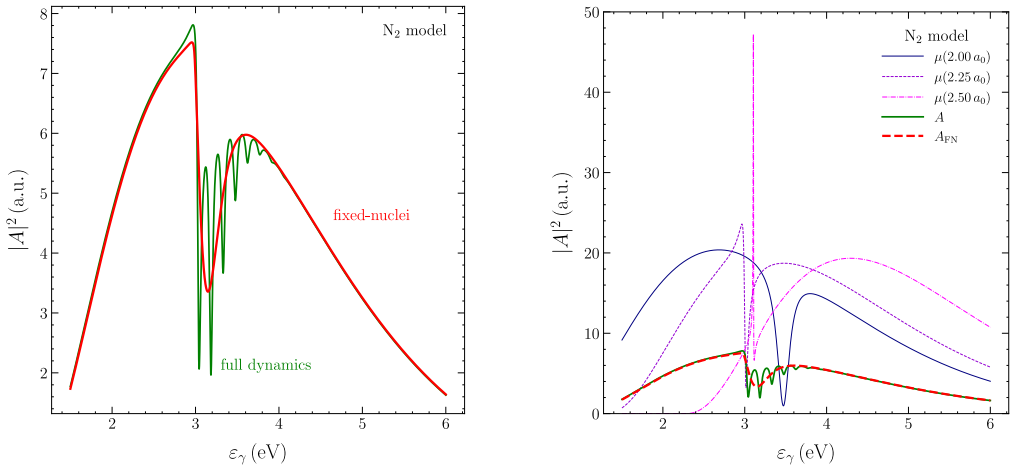

Figure 3.8 Energy dependence of the squared photodetachment amplitude $|A|^2$ for the N_2 model, comparing the amplitude computed with full dynamics against the fixed-nuclei approximation. The right graph additionally includes the fixed-R moment function μ for various R values.

amplitude calculated using complete dynamics and the fixed-nuclei approximation. Here, it is evident that the fixed-nuclei approximation fails to describe the boomerang oscillations in the photodetachment process, as expected, because these oscillations are inherently linked to the nuclear dynamics, which is ignored in the fixed-nuclei approximation. This figure illustrates that although the fixed-nuclei approximation accurately captures the resonance energy peak, it smooths over the boomerang oscillations, averaging out their effects instead of displaying them.

On the second graph in Fig. 3.8, we additionally plot the fixed-R moment function μ for three different values of R. Compared to the LiH model, here the moment function μ exhibits much more erratic behavior even for closely spaced values of R.

Conclusion

In this thesis, we successfully developed numerical methods to compute the amplitudes of the resonant photodetachment process. We utilized the discrete-state-in-continuum model and projection operator formalism, generally used to describe low-energy inelastic electron collisions with molecules leading to vibrational excitation. Additionally, we introduced the fixed-nuclei approximation, which simplifies the resonance photodetachment process by neglecting the nuclear dynamics.

We thoroughly described the implementation of each numerical procedure for general applicability. Our computations were specifically implemented in FORTRAN 90, utilizing the LAPACK library for commonly used numerical procedures. The developed numerical methods were rigorously tested for each studied model.

In our study, we focused only on diatomic molecules and implemented several simplifications. We assumed only one energetically accessible electronic state of the neutral molecule and only one discrete metastable state. Additionally, only the first partial wave of the outgoing electron was accounted for. However, we see no obstacles in releasing these assumptions to study more complex systems in future work.

Firstly, we applied the numerical methods to a model inspired by the LiH molecule, which was the primary model on which the methods were developed. We examined the amplitude of the photodetachment process while providing a physical explanation of different components contributing to the full amplitude. We observed a peak in the amplitude corresponding to the resonance energy directly linked to the energy difference between the potential wells of the stable and metastable anion states. In this model, we also studied how the resonance mitigates the decline in photodetachment amplitude for higher final vibrational states of the neutral molecule. Near this resonance energy, the decline in amplitude for higher vibrational states was found to be comparable to vibrational excitation by electron scattering, whereas outside of this resonance region, the process was dominated by the rapidly decreasing direct term.

Secondly, we investigated the N_2-inspired model in search of a process similar to the *boomerang oscillations*, a phenomenon observed in vibrational excitation by electron scattering cross-sections of the N_2 molecule. In the numerical calculations for this model, which tested the developed methods in another regime, we indeed observed similar oscillations, proving the existence of this analog, at least in our simplified models. Additionally, for the same N_2-inspired model, we calculated the vibrational excitations using our numerical methods and found that the results qualitatively agreed with those reported in the scientific literature.

The fixed-nuclei approximation was quite successful in describing the amplitudes of the photodetachment process for our LiH-inspired model. It also provided us with a unique insight that the final energy dependence curve of the photodetachment amplitude results from broadening the fixed-nuclei moment functions across the distribution of nuclei determined by their vibrational wavefunction. However, we also observed the limitations of this approximation. The fixed-nuclei approach completely failed to describe the boomerang oscillations, a phenomenon fully governed by nuclear dynamics, in the photodetachment process for our N_2 model.

In the future, we aim to use the developed numerical methods on other molecular models. We would like to find analogs in the resonance photodetachment of other phenomena observed in inelastic electron-molecule collisions, such as threshold peaks and Wigner cusps.

Bibliography

[1] Domcke, W. "Theory of resonance and threshold effects in electron-molecule collisions: The projection-operator approach". In: *Physics Reports* 208.2 (1991), pp. 97–188. ISSN: 0370-1573. DOI: https://doi.org/10.1016/0370-1573(91)90125-6.

[2] Houfek, K., Čížek, M., and Horáček, J. "On irregular oscillatory structures in resonant vibrational excitation cross-sections in diatomic molecules". In: *Chemical Physics* 347 (May 2008), pp. 250–256. DOI: 10.1016/j.chemphys.2007.11.017.

[3] Čížek, M. *Photodetachment dynamics using nonlocal dicrete-state-in-continuum model*. 2023. arXiv: 2309.05830 [physics.chem-ph].

[4] LAPACK Developers. *LAPACK - Linear Algebra Package*. Included in Intel Fortran Composer. Version included with Intel Fortran Composer 2013, accessed 2023. 2023. URL: http://www.netlib.org/lapack/.

[5] Fornberg, B. "Generation of Finite Difference Formulas on Arbitrarily Spaced Grids". In: *Mathematics of Computation* 51.184 (1988), pp. 699–706. DOI: 10.1090/S0025-5718-1988-0935077-0.

[6] Horáček, J., Gemperle, F., and Meyer, H. "Calculation of dissociative attachment of electrons to diatomic molecules by the Schwinger–Lanczos approach". In: *The Journal of Chemical Physics* 104.21 (June 1996), pp. 8433–8441. ISSN: 0021-9606. DOI: 10.1063/1.471593.

[7] Cejnar, P. *A Condensed Course of Quantum Mechanics*. 1st ed. Page 32. Prague: Karolinum Press, Charles University, 2013.

[8] Černý, R. and Pokorný, M. *Základy matematické analýzy pro studenty fyziky II*. 1st ed. Lemma 8.5.8. Praha: Matfyzpress, 2021. Chap. 8. ISBN: 978-80-7378-454-6.

[9] Koonin, S. E. *Computational Physics: Fortran Version*. Reading, MA: Addison-Wesley, 1998. ISBN: 978-0201386233.

[10] Černý, R. and Pokorný, M. *Základy matematické analýzy pro studenty fyziky IV*. 1st ed. Příklad 23.5.9. Prague: Matfyzpress, 2024. Chap. 23. ISBN: 978-80-7378-509-3.

[11] Čížek, M. "Resonant processes in atomic collisions: Theoretical considerations and calculations". Appendix B. Ph.D. Dissertation. Prague: Charles University, 1999.

[12] Dahl, J. P. and Springborg, M. "The Morse oscillator in position space, momentum space, and phase space". In: *The Journal of Chemical Physics* 88.7 (Apr. 1988), pp. 4535–4547. ISSN: 0021-9606. DOI: 10.1063/1.453761.

Appendix A

Molecular models

In this appendix, we describe the molecular models used in this thesis. It is important to note that these models are significantly simplified and are intended to provide qualitative insights into molecular dynamics rather than precise quantitative predictions. These models are largely adapted from existing literature, particularly from the work of my supervisor [3]. The thesis focuses solely on describing the photodetachment process in diatomic molecules. The models for different molecules are largely described by the same functions, although their parameters vary across different models.

As outlined in previous chapters, our calculations of the photodetachment process require knowledge of the following potential curves: the potential of the neutral molecule $W(R)$, the potential of the ground anionic state $V_0(R)$, and the potential of the electronically excited state $V_1(R)$. Additionally, we need information on the discrete-state-in-continuum coupling function $V_{1\epsilon}(R)$ and the fixed-R transition dipole moments for the discrete state $\mu_1(R)$ and for the background continuum $\mu_\epsilon(R)$.

To model the potential curves $W(R)$ and $V_0(R)$, we use a Morse potential. For the discrete-state-in-continuum $V_1(R)$, we have opted to describe it using a more general function. These functions are defined as follows:

$$W(R) = d_W e^{-2a_W(R-R_W)} - 2d_W e^{-a_W(R-R_W)} + b_W, \tag{A.1}$$

$$V_0(R) = d_0 e^{-2a_0(R-R_0)} - 2d_0 e^{-a_0(R-R_0)} + b_0, \tag{A.2}$$

$$V_1(R) = d_1 e^{-a_1(R-R_1)} + \delta_1 e^{-\alpha_1(R-\rho_1)}. \tag{A.3}$$

The discrete-state potential $V_1(R)$ and its coupling function $V_{1\epsilon}(R)$ are usually selected to correspond with the fixed-nuclei scattering phase-shift, as detailed in [3]. As discussed in Sections 2.1 and 2.2.3, it is crucial for our numerical methods that the discrete-state-in-continuum $V_{1\epsilon}(R)$ assumes a

separable form and its energy dependence is in a special form as follows:

$$V_{1\epsilon}(R) = g(R)f(\epsilon), \tag{A.4}$$

$$\gamma(\epsilon) \coloneqq 2\pi f^2(\epsilon) = A_\gamma \left[\tfrac{\epsilon}{B_\gamma}\right]^\alpha \exp\left[-\tfrac{\epsilon}{B_\gamma}\right]. \tag{A.5}$$

The function $g(R)$, which describes the radial-coordinate dependence, is uniquely defined for each model.

Lastly, the fixed-R transition dipole moments are also inspired by fixed-nuclei scattering calculations for each model [3]. As mentioned in Section 2.1, the transition dipole moment to the background continuum must assume a separable form. However, in our simplified models, we entirely omit its radial dependence. From Section 2.2.3, it is again necessary that its energy dependence follows a specified functional form

$$\gamma_\mu(\epsilon) \coloneqq 2\pi f_\mu^2(\epsilon) \equiv 2\pi\mu_\epsilon^2 = A_\mu \left[\tfrac{\epsilon}{B_\mu}\right]^\alpha \exp\left[-\tfrac{\epsilon}{B_\mu}\right]. \tag{A.6}$$

Furthermore, for the transition dipole moment to the discrete state, the radial dependence is also omitted, and we choose a complex number with a non-trivial phase [3]

$$\mu_1 = 0.1 + 0.1i. \tag{A.7}$$

Here, we define the radial-coordinate dependence of the discrete-state-in-continuum coupling function $V_{1\epsilon}(R)$ for the various models, where R is always given in Bohrs (a_0).

LiH model:

$$g_{\mathrm{LiH}}(R) = \left[1 + e^{0.75(R-6)}\right]^{-1} \tag{A.8}$$

N_2 model:

$$g_{\mathrm{N_2}}(R) = e^{-1.5(R-2.0787)} \tag{A.9}$$

	LiH model	N_2 model
$W(R)$ potential curve		
d_W (eV)	2.5	12.2
a_W $(1/a_0)$	0.6	1.16419
R_W (a_0)	3.0	2.0787
b_W (eV)	0.57	-1.07
$V_0(R)$ potential curve		
d_0 (eV)	2.1	8.0
a_0 $(1/a_0)$	0.45	0.914033
R_0 (a_0)	3.1	2.2
b_0 (eV)	-0.13	-6.17
$V_1(R)$ potential curve		
d_1 (eV)	1.9	11.1
δ_1 (eV)	0.0	-22.2
a_1 $(1/a_0)$	0.6	1.9339
α_1 $(1/a_0)$	–	0.96695
R_1 (a_0)	3.0	2.24877
ρ_1 (a_0)	–	2.24877
$f(\epsilon)$ and μ_ϵ		
A_γ (eV)	1.0	0.25
B_γ (eV)	2.0	2.0
A_μ (a.u.)	150	150
B_μ (eV)	0.8	0.8
α	0.2	2.5

Table A.1 Parameters of the molecular models for different diatomic molecules, specifically LiH and N_2. The table lists values for various parameters defining the potential curves $W(R)$, $V_0(R)$, and $V_1(R)$, and also energy dependence of discrete-state-in-continuum coupling function $f(\epsilon)$ and fixed-R transition dipole moment to the background continuum μ_ϵ

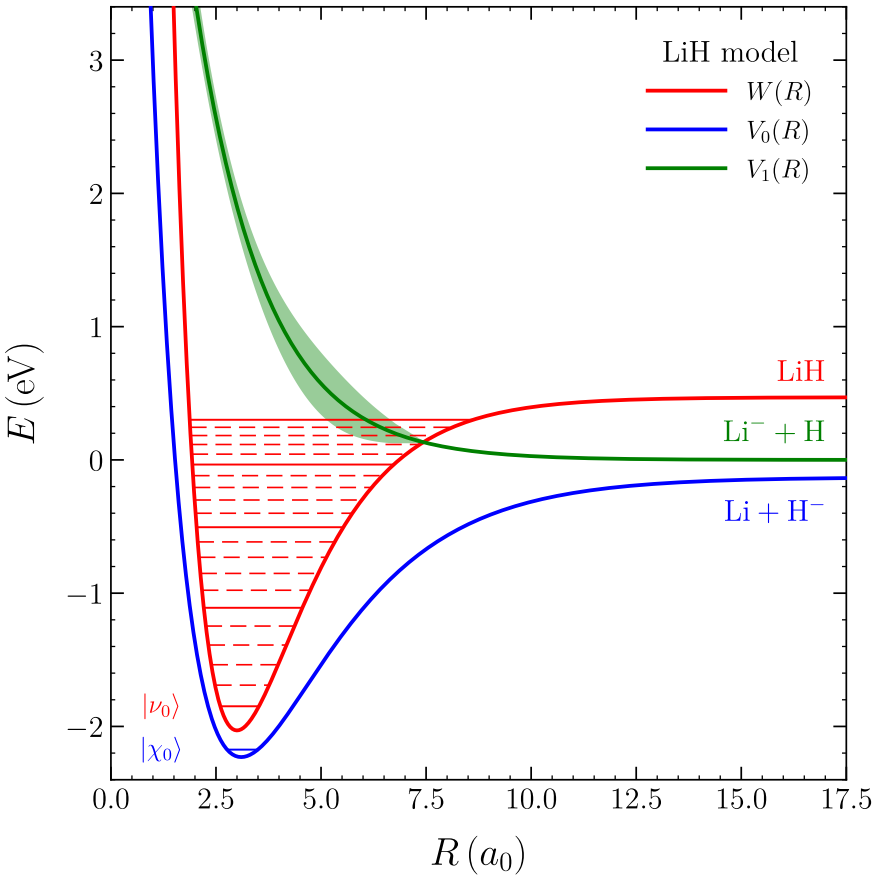

Figure A.1 Schematic of the model inspired by the LiH molecule. This graph displays the potential curves for the neutral molecule $W(R)$, the ground state of the anion $V_0(R)$, and the electronically excited anion $V_1(R)$, which includes a depiction of the resonance width, as functions of the internuclear distance R in atomic units (a_0).

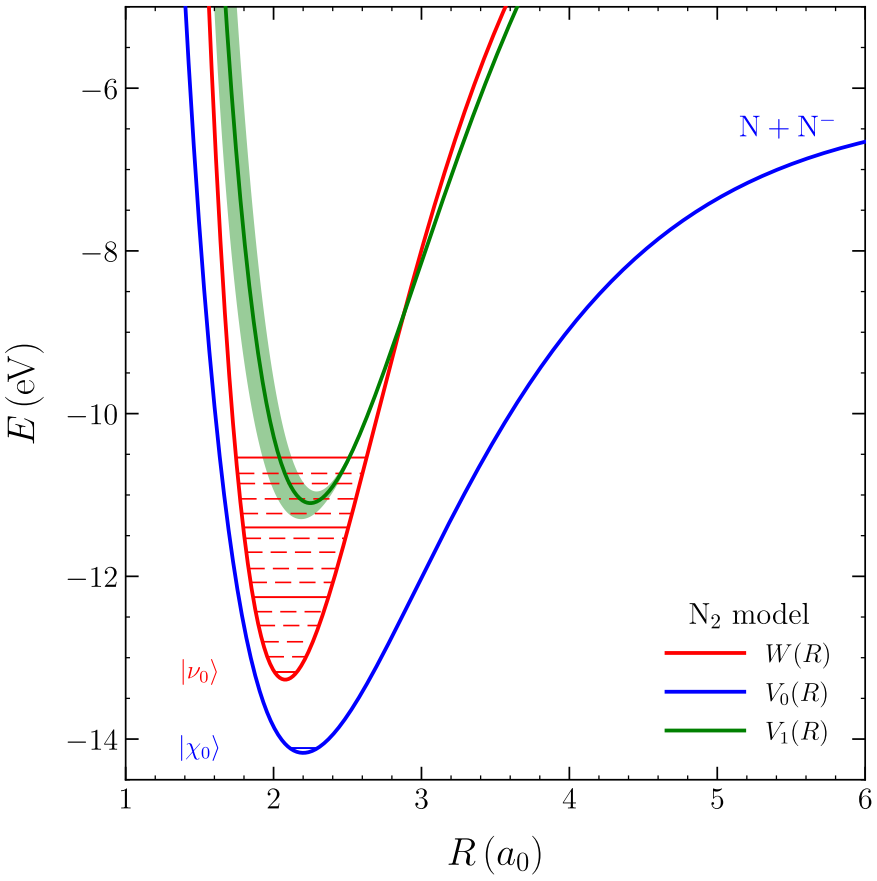

Figure A.2 Schematic of the model inspired by the N_2 molecule. This graph displays the potential curves for the neutral molecule $W(R)$, the ground state of the anion $V_0(R)$, and the electronically excited anion $V_1(R)$, which includes a depiction of the resonance width, as functions of the internuclear distance R in atomic units (a_0).

Appendix B

Convergence analysis data

This appendix provides detailed tables related to the convergence analysis described in Section 2.3.4. The convergence of numerical results for photodetachment amplitudes and vibrational excitation amplitudes was assessed across a range of computational parameters. As outlined, the stability and accuracy of the results were verified by systematic variations in key numerical parameters, ensuring the reliability of our findings within the studied energy range. For clarity, we present data only for the ground final state $|\nu_0\rangle$, which corresponds to η_0, and the last discussed final state $|\nu_j\rangle$ for each model, which corresponds to η_j. The index j represents the last vibrational state discussed in Section 3, and may vary across different models. Deviations for states between these extremes were generally within the range established by these endpoints. Therefore, for clarity, we only present the first and last state, showcasing the spread of precision across the spectrum. The following sections provide a clear presentation of the data, documenting the convergence tests for different models detailed in Appendix A.

In the tables provided, the symbol # denotes the run number, and the values of R_N are specified in atomic units (Bohrs). The relative deviations η are presented as percentages to facilitate a clear understanding of the variations in precision across different computational runs. This format helps in directly comparing the impact of parameter adjustments on the convergence of our results.

LiH model

#	R_N	N	n_κ	N_{DVR}	t	$\overline{\eta}_0$	$\eta_0^{\max}$	$\overline{\eta}_{20}$	$\eta_{20}^{\max}$
1	11.0	1 100	80	110	2	–	–	–	–
2	12.0	1 400	95	130	3	0.021	0.149	0.304	2.651
3	13.0	1 700	110	150	3	0.014	0.107	0.232	2.584
4	14.0	2 000	125	170	3	0.010	0.084	0.186	1.957
5	15.0	2 300	140	190	3	0.007	0.067	0.158	2.440
6	16.0	2 600	155	210	3	0.006	0.063	0.137	2.628
7	17.0	2 900	170	230	3	0.005	0.045	0.115	1.287
8	18.0	3 200	185	250	3	0.004	0.056	0.103	1.093

Table B.1 Convergence Data for Photodetachment Amplitudes (A) for the LiH Model. Relative deviations η are shown as percentages, with R_N values provided in Bohrs.

#	R_N	N	n_κ	N_{DVR}	t	$\overline{\eta}_0$	$\eta_0^{\max}$	$\overline{\eta}_{20}$	$\eta_{20}^{\max}$
1	11.0	1 100	80	110	2	–	–	–	–
2	12.0	1 400	95	130	3	0.070	0.206	0.367	2.938
3	13.0	1 700	110	150	3	0.042	0.181	0.275	2.967
4	14.0	2 000	125	170	3	0.028	0.112	0.225	2.174
5	15.0	2 300	140	190	3	0.020	0.106	0.191	2.394
6	16.0	2 600	155	210	3	0.015	0.096	0.163	2.568
7	17.0	2 900	170	230	3	0.012	0.089	0.139	1.302
8	18.0	3 200	185	250	3	0.010	0.077	0.122	1.277

Table B.2 Convergence Data for Vibrational Excitation Amplitudes (T_{VE}) for the LiH Model. Relative deviations η are shown as percentages, with R_N values provided in Bohrs.

N_2 model

#	R_N	N	n_κ	N_{DVR}	t	$\overline{\eta}_0$	$\eta_0^{\max}$	$\overline{\eta}_2$	$\eta_2^{\max}$
1	10.0	1 000	80	110	1	–	–	–	–
2	10.5	1 300	95	130	2	1.395	6.117	62.564	77.667
3	11.0	1 600	110	150	2	0.223	4.242	17.715	27.556
4	11.5	1 900	125	170	2	0.073	1.601	4.566	5.817
5	12.0	2 200	145	195	2	0.025	0.793	0.614	2.252
6	12.5	2 500	165	220	2	0.014	0.444	0.125	1.038
7	13.0	2 800	185	245	2	0.009	0.268	0.018	0.537

Table B.3 Convergence Data for Photodetachment Amplitudes (A) for the N_2 Model. Relative deviations η are shown as percentages, with R_N values provided in Bohrs.

#	R_N	N	n_κ	N_{DVR}	t	$\overline{\eta}_0$	$\eta_0^{\max}$	$\overline{\eta}_2$	$\eta_2^{\max}$
1	10.0	1 000	80	110	1	–	–	–	–
2	10.5	1 300	95	130	2	5.949	154.665	53.919	9894.866
3	11.0	1 600	110	150	2	2.134	31.191	18.183	554.448
4	11.5	1 900	125	170	2	1.001	10.347	9.766	168.704
5	12.0	2 200	145	195	2	0.526	3.916	3.584	140.576
6	12.5	2 500	165	220	2	0.266	0.874	1.250	29.334
7	13.0	2 800	185	245	2	0.144	0.606	0.642	3.396

Table B.4 Convergence Data for Vibrational Excitation Amplitudes (T_{VE}) for the N_2 Model. Relative deviations η are shown as percentages, with R_N values provided in Bohrs.